Effects of passive dendritic tree properties on the firing dynamics of a leaky-integrate-and-fire neuron

Abulhair Saparov [a,*], Michael A. Schwemmer [b]

[a] *Machine Learning Department, Carnegie Mellon University, Pittsburgh, PA, USA*
[b] *Mathematical Biosciences Institute, The Ohio State University, Columbus, OH, USA*

ARTICLE INFO

ABSTRACT

We study the effects of dendritic tree topology and biophysical properties on the firing dynamics of a leaky-integrate-and-fire (LIF) neuron that explicitly includes spiking dynamics. We model the dendrites as a multi-compartment tree with passive dynamics. Owing to the simplicity of the system, we obtain the full analytical solution for the model which we use to derive a lower dimensional return map that captures the complete dynamics of the system. Using the map, we explore how biophysical properties and dendritic tree architecture affect firing dynamics. As was first reported in earlier work by one of the authors, we also find that the addition of the dendritic tree can induce bistability between periodic firing and quiescence. However, we go beyond their results by systematically examining how dendritic tree topology affects the appearance of this bistable behavior. We find that the structure of the dendritic tree can have significant quantitative effects on the bifurcation structure of the system, with branchier topologies tending to promote bistable behavior over unbranched chain topologies. We also show that this effect occurs even when the input conductance at the soma is held fixed, indicating that the topology of the dendritic tree is mainly responsible for this quantitative change in the bifurcation structure. Lastly, we demonstrate how our framework can be used to explore the effect of biophysical properties on the firing dynamics of a neuron with a more complex dendritic tree topology.

© 2015 Elsevier Inc. All rights reserved.

1. Introduction

Neurons can have extensive spatial geometries, but are typically modeled as single compartment objects, with no explicit spatial dependence. This modeling choice is often made for mathematical tractability and/or computational efficiency. However, many neurons are not electrotonically compact, and single compartment models cannot be expected to capture the full range of dynamical behaviors of neurons. Dendrites (the branched structures emanating from the cell body, or soma) can substantially affect the electrical activity of single neurons. For instance, the types of ion channels and their density along the dendritic tree can alter the firing patterns of neurons [1–3]. Even dendrites endowed with passive (linear) ion channels can alter the frequency and firing dynamics of neurons in interesting and sometimes counter-intuitive ways [4–6]. Thus, a full understanding of these neural firing behaviors requires the analysis of more detailed models.

The effects of dendritic tree architecture on the electrical activity of neurons were first explored by Rall, who demonstrated that each segment of the tree can be effectively modeled as a one-dimensional cable [7–9]. However, mathematical analysis on the resulting system of coupled one-dimensional partial differential equations quickly becomes intractable once nonlinear ionic currents are included in the dendrites. In this case, various computational studies have shown that the interaction of dendritic topology and the nonlinear ionic currents affect both the firing frequency and the type of firing (regular, bursting) in neurons, e.g., [2,3,10]. Alternatively, when the dynamics of each of the dendritic tree segments is linear or quasi-linear, a Green's function can be derived which captures how the architecture of the tree affects the filtering of a current stimulus input to the dendrite [11–13]. Although the Green's function approach allows for a large reduction in computational complexity in exploring how the membrane potential of dendritic trees responds to time-varying inputs, these approaches assume linearity, which prohibits the inclusion of any nonlinear spike-generating mechanisms. As such, Green's function approaches are limited in their applicability to exploring how dendritic topology affects neuronal firing dynamics.

Recently, Schwemmer and Lewis were able to explore the effects of passive dendritic properties on the dynamics of a leaky-integrate-

and-fire (LIF) model neuron [14] that explicitly includes spike effects [6]. Owing to the simplicity of the LIF neuron, they were able to obtain the analytical solution of the system, which they used to show that the inclusion of the dendrite sometimes caused the system to display bistability between periodic oscillations and quiescence, reminiscent of Hodgkins' type 2 excitability [15]. However, as the dendrite was modeled as a single one-dimensional passive cable, the branching structure of the dendritic tree is ignored. Here, we extend the results of [6] in order to explore how the topology of a passive dendritic tree affects the firing dynamics of the LIF neuron. To accomplish this, we model the dendritic tree as a system of n ordinary differential equations connected by electronic coupling, i.e., each segment of the dendritic tree is now assumed to be a single isopotential compartment [16]. The soma is again modeled using LIF dynamics that explicitly include spike effects. Owing to the simplicity of the system, we are able to obtain the full analytical solution to the $n + 1$-dimensional system, and use it to derive an n-dimensional return map which captures the dynamics of the full system. Using this framework, we seek to understand how dendritic tree properties alter firing dynamics. In particular, we systematically explore how the interaction of dendritic biophysical properties and dendritic tree structure affect the appearance of the bistable behavior that was previously reported in [6]. We find that dendritic topology has a strong quantitative affect on the bifurcation structure of the system, with more complex, branchier dendritic tree topologies tending to promote bistability.

This paper is organized as follows. In Section 2, we describe our multi-compartment LIF model. We then show how one can analytically derive the solution to the system, and use the solution to construct the return map. Using the return map, we systematically explore how biophysical parameters interact with simplified dendritic topologies to affect firing dynamics. We find that dendritic topology has a strong quantitative affect on the bifurcation structure of the system. Lastly, we demonstrate the flexibility of the model by exploring the firing dynamics of a neuron with a more complex dendritic topology.

2. Multi-compartment leaky-integrate-and-fire model

We model a neuron as an isopotential somatic compartment electrically coupled to a passive dendritic tree. As opposed to other approaches that have modeled the dendritic tree using a series of coupled passive cables (e.g., [8,13]) or a single equivalent cylinder (e.g., [6]), we choose to model the tree as a series of coupled isopotential compartments, i.e., a multi-compartment model (e.g., [16–18]). This greatly simplifies the analysis while still allowing us to explore the effects of dendritic architecture on the firing dynamics of the system. The somatic dynamics are described by a leaky-integrate-and-fire (LIF) model that explicitly includes a spike [6,14] while each of the n dendritic compartments contains passive (linear) dynamics. For concreteness, we initially focus on two specific dendritic topologies. We refer to the first topology as the "branch" model, where all n dendrites are attached to the soma and nothing else. The second topology will be referred to as the "chain" model and consists of the soma connected to a linear chain of dendritic compartments, with each compartment being connected to at most two other compartments.

2.1. Somatic dynamics

The non-spiking dynamics of the membrane potential of the somatic compartment $\bar{V}_S(\bar{t})$ are given by

$$C_m \frac{d\bar{V}_S}{d\bar{t}} = -g_{LS}(\bar{V}_S - E_{LS}) + \bar{I}_S + \bar{I}_{coupl}^D(t), \tag{1}$$

where C_m is the membrane capacitance, g_{LS} is the somatic leakage conductance, E_{LS} is the somatic leakage reversal potential, $\bar{I}_S$ is the external current applied to the soma, and $\bar{I}_{coupl}^D(t)$ is the current flowing

from the dendritic tree into the soma. The specific form of $\bar{I}_{coupl}^D(t)$ depends on the architecture of the dendritic tree, and we will discuss two example cases in the sections that follow. When $\bar{V}_S$ reaches a threshold voltage $\bar{V}_{th}$ at time $\bar{t} = \bar{t}_s^j$ ($\bar{V}_S(\bar{t}_s^j) = \bar{V}_{th}$) the jth spike is elicited in the soma. During the spike, the somatic potential is given by

$$\bar{V}_S(\bar{t}) = \bar{h}(\bar{t} - \bar{t}_s^j), \ \bar{t} \in (\bar{t}_s^j, \bar{t}_s^j + \bar{T}_a], \tag{2}$$

where $\bar{h}(\bar{t})$ is a function that describes the shape of the somatic spike. More specifically, $\bar{h}(\bar{t})$ is a continuous function that takes the somatic potential from the maximum spike height $\bar{h}(0) = \bar{H}$ to the reset potential at the end of the spike $\bar{h}(\bar{T}_a) = \bar{V}_R$ (see Section 3.1 for a discussion of the specific types of spike shapes we use). After a time $\bar{T}_a$, the somatic dynamics are switched back to (1) at $\bar{t} = \bar{t}_s^j + \bar{T}_a$. Thus, $\bar{T}_a$ represents the temporal duration of the somatic spike.

In the next two sections, we describe the dynamics of the dendritic compartments. In particular, we describe the branch and chain models in detail. However, in the Appendix, we show how this framework can be applied to any arbitrary topology for the dendritic tree.

2.1.1. Branch model

In the branch model, all n dendritic compartments are coupled directly to the soma, and no coupling exists between the dendritic compartments. Let $\bar{V}_i$ denote the membrane potential of the ith dendritic compartment. The dynamics are then given by

$$C_m \frac{d\bar{V}_i}{d\bar{t}} = -g_{LD_i}(\bar{V}_i - E_{LD_i}) + \bar{I}_i + \frac{g_{C_i}}{A_i}(\bar{V}_S - \bar{V}_i), \tag{3}$$

where g_{LD_i} is the leakage conductance, E_{LD_i} is the leakage reversal potential, $\bar{I}_i$ is the external current, g_{C_i} is the coupling conductance measured in mS, and A_i is the surface area of the dendritic compartment measured in cm². In this case, the current flowing from the dendritic tree into the soma is given by

$$\bar{I}_{coupl}^D(t) = \sum_{i=1}^{n} \frac{g_{C_i}}{A_S}(\bar{V}_i - \bar{V}_S), \tag{4}$$

where A_S is the area of the somatic compartment.

2.1.2. Chain model

In the chain model, we have a different set of differential equations. Note that the first $n - 1$ dendrites are connected to both the preceding and subsequent dendrites, and the nth dendrite is only connected to the previous compartment. Using the notation above, we write the equation for the voltage of dendrite $i \in \{2, \ldots, n - 1\}$:

$$C_m \frac{d\bar{V}_i}{d\bar{t}} = -g_{LD_i}(\bar{V}_i - E_{LD_i}) + \bar{I}_i + \frac{g_{C_i}}{A_i}(\bar{V}_{i-1} - \bar{V}_i) + \frac{g_{C_{i+1}}}{A_i}(\bar{V}_{i+1} - \bar{V}_i). \tag{5}$$

For the dendrites at the ends, we have:

$$C_m \frac{d\bar{V}_1}{d\bar{t}} = -g_{LD_1}(\bar{V}_1 - E_{LD_1}) + \bar{I}_1 + \frac{g_{C_1}}{A_1}(\bar{V}_S - \bar{V}_1) + \frac{g_{C_2}}{A_1}(\bar{V}_2 - \bar{V}_1),$$

$$C_m \frac{d\bar{V}_n}{d\bar{t}} = -g_{LD_n}(\bar{V}_n - E_{LD_n}) + \bar{I}_n + \frac{g_{C_n}}{A_n}(\bar{V}_{n-1} - \bar{V}_n). \tag{6}$$

In this case, the current flowing from the dendritic tree into the soma is given by

$$\bar{I}_{coupl}^D(t) = \frac{g_{C_1}}{A_S}(\bar{V}_1 - \bar{V}_S). \tag{7}$$

For convenience, we list all model parameters along with their physical interpretations in Table 1.

Table 1
List of dimensional parameters.

Dimensional parameters			
C_m	Membrane capacitance	g_{LS}	Somatic leakage conductance
$\bar{I}_i$	Current injected into dendrite i	E_{LD_i}	Dendritic leakage reversal potential
$\bar{I}_S$	Current injected into the soma	E_{LS}	Somatic leakage reversal potential
$\bar{V}_i$	Membrane potential of dendrite i	A_i	Surface area of dendrite i
$\bar{V}_S$	Somatic membrane potential	A_S	Somatic surface area
$\bar{t}$	Dimensional time	g_{C_i}	Coupling conductance
g_{LD_i}	Dendritic leakage conductance		

Table 2
List of nondimensional parameters.

Nondimensional parameters	
V_i	Normalized membrane potential of dendrite i
V_S	Normalized somatic membrane potential
β_i	Normalized leakage reversal potential of dendrite i
β_S	Normalized leakage reversal potential of the soma
I_i	Normalized current injected into dendrite i
I_S	Normalized current injected into the soma
α_i	Ratio of surface area of the soma to the area of dendrite i
γ_i	Ratio of leakage conductance of dendrite i to dendrite 1
γ_S	Ratio of somatic leakage conductance to dendrite 1
g_i	Normalized coupling conductance

2.2. Nondimensionalization

For ease of mathematical analysis, we nondimensionalize the system using the following substitutions, with $i = 1, 2, \ldots, n$:

$$V_S(t) = \frac{\bar{V}_S(\bar{t}/\tau_1) - E_{LD_1}}{\bar{V}_{th} - E_{LD_1}}, \; V_i(t) = \frac{\bar{V}_i(\bar{t}/\tau_1) - E_{LD_1}}{\bar{V}_{th} - E_{LD_1}}, \; \beta_S = \frac{E_{LS} - E_{LD_1}}{\bar{V}_{th} - E_{LD_1}},$$

$$\beta_i = \frac{E_{LD_i} - E_{LD_1}}{\bar{V}_{th} - E_{LD_1}}, \; I_S = \frac{\bar{I}_S}{g_{LD_1}(\bar{V}_{th} - E_{LD_1})}, \; I_i = \frac{\bar{I}_i}{g_{LD_1}(\bar{V}_{th} - E_{LD_1})},$$

$$\tau_S = \frac{C_m}{g_{LS}}, \; \tau_i = \frac{C_m}{g_{LD_i}}, \; \alpha_i = \frac{A_S}{A_i}, \; \gamma_S = \frac{g_{LS}}{g_{LD_1}}, \; \gamma_i = \frac{g_{LD_i}}{g_{LD_1}}, \; g_i = \frac{g_{C_i}}{A_S g_{LD_1}}.$$

With the above scalings, we have $V_{th} = 1$, $\beta_1 = 0$, and $\gamma_1 = 1$. All nondimensional parameters are also listed along with their interpretation in Table 2.

Applying the above scalings, we arrive at the equations for the nondimensional somatic voltage dynamics

$$\begin{cases} \dfrac{dV_S}{dt} = -\gamma_S(V_S - \beta_S) + I_S + I_{coupl}^D(t) & \text{if } t \notin (t_s^j, t_s^j + T_a], \\ V_S(t) = h(t - t_s^j) & \text{if } t \in (t_s^j, t_s^j + T_a], \end{cases} \quad (8)$$

where $t_s^j = \bar{t}_s^s/\tau_1$, $T_a = \bar{T}_a/\tau_1$, and $h(t) = (\bar{h}(\bar{t}/\tau_1) - E_{LD_1})/(\bar{V}_{th} - E_{LD_1})$. Similarly, $H = (\bar{H} - E_{LD_1})/(\bar{V}_{th} - E_{LD_1})$ and $V_R = (\bar{V}_R - E_{LD_1})/(\bar{V}_{th} - E_{LD_1})$ are the nondimensional height of the somatic spike and reset potential, respectively. We call a set of parameters *biophysically-plausible* if all conductances and areas are strictly positive.

2.2.1. Branch model
Applying these transformations to the dimensional representation of the branch model yields the following equation for the dynamics of the nondimensional dendritic voltages

$$\frac{dV_i}{dt} = -\gamma_i(V_i - \beta_i) + I_i + \alpha_i g_i(V_S - V_i). \quad (9)$$

The nondimensional current flowing from the dendritic tree into the soma is given by

$$I_{coupl}^D = \sum_{i=1}^{n} g_i(V_i - V_S). \quad (10)$$

2.2.2. Chain model
For the chain model, the dynamics of the nondimensional dendritic voltages are given by

$$\frac{dV_1}{dt} = -V_1 + I_1 + \alpha_1 g_1(V_S - V_1) + \alpha_1 g_2(V_2 - V_1), \quad (11)$$

$$\frac{dV_i}{dt} = -\gamma_i(V_i - \beta_i) + I_i + \alpha_i g_i(V_{i-1} - V_i)$$
$$+ \alpha_i g_{i+1}(V_{i+1} - V_i), \; i = 2, \ldots, n-1,$$

$$\frac{dV_n}{dt} = -\gamma_n(V_n - \beta_n) + I_n + \alpha_n g_n(V_{n-1} - V_n).$$

The nondimensional current flowing from the dendritic tree into the soma is given by

$$I_{coupl}^D = g_1(V_1 - V_S). \quad (12)$$

2.3. Matrix formulation

The above dimensional and nondimensional systems can be conveniently represented in matrix form. Let $\mathbf{V}$ be a vector where the first n elements represent the nondimensional dendritic voltage V_i, and the $(n+1)$th element represents the nondimensional somatic voltage V_S:

$$\mathbf{V} = \begin{bmatrix} V_1 \\ \vdots \\ V_n \\ V_S \end{bmatrix} \quad (13)$$

This matrix formulation is sufficiently general to represent any dendritic topology, and we will conduct much of our analysis in this form. We are able to re-write the nondimensionalized system of differential equations for both the branch and chain topologies in the following form:

$$\frac{d\mathbf{V}}{dt} = A^{NS}\mathbf{V} + \mathbf{b}^{NS}, \quad (14)$$

where NS refers to the fact that this is the evolution of the voltage when the system is not spiking, A^{NS} is an $(n+1) \times (n+1)$ matrix of coefficients, and $\mathbf{b}^{NS}$ is a $(n+1) \times 1$ vector of constants. Similarly, we re-write the spiking system in matrix form:

$$\begin{cases} \dfrac{d\mathbf{V}_D}{dt} = A^S\mathbf{V}_D + \mathbf{b}^S(t - t_s^j), \\ V_S(t) = h(t - t_s^j), \end{cases} \quad (15)$$

where $\mathbf{V}_D$ is an n-dimensional vector of nondimensional dendritic membrane potentials. Here, A^S is the top-left $n \times n$ submatrix of A^{NS}, and has one fewer row and column since the differential equation no longer governs the somatic voltage. The dependency on the somatic voltage is moved into the vector $\mathbf{b}^S(t)$.

Regardless of the topology, we find that the multi-compartment LIF neuron displays two types of stable characteristic behavior depending on parameters: (i) time independent steady-states, and (ii) steady periodic oscillations.

2.4. Matrix formulation of branch and chain models

For concreteness, we provide the matrix formulation of both the branch and chain models. That is, we specify A^{NS}, A^S, $\mathbf{b}^{NS}$, and $\mathbf{b}^S(t)$ as described by Eqs. (14) and (15). However, we emphasize that our model can be applied to any dendritic architecture (see Section A.1). Additionally, in Section A.1, we show that for biophysically-plausible settings of the parameters and for dendritic architectures where the corresponding graph of compartments has no cycles, the eigenvalues of the A^{NS} and A^S matrices will always be real and strictly negative.

2.4.1. Branch model

When the system is not spiking, the matrix A^{NS} and vector $\mathbf{b}^{NS}$ for the branch model are given by

$$
A^{NS}_{branch} =
\begin{bmatrix}
-1-\alpha_1 g_1 & 0 & 0 & \cdots & \alpha_1 g_1 \\
0 & -\gamma_2-\alpha_2 g_2 & 0 & \cdots & \alpha_2 g_2 \\
0 & 0 & -\gamma_3-\alpha_3 g_3 & \cdots & \alpha_3 g_3 \\
\vdots & \vdots & \vdots & \ddots & \vdots \\
0 & 0 & 0 & \cdots & \alpha_n g_n \\
g_1 & g_2 & g_3 & \cdots & -\gamma_S-\sum_{i=1}^{n} g_i
\end{bmatrix}
$$

$$
\text{and} \quad \mathbf{b}^{NS}_{branch} =
\begin{bmatrix}
I_1 \\
\gamma_2 \beta_2 + I_2 \\
\vdots \\
\gamma_S \beta_S + I_S
\end{bmatrix}. \tag{16}
$$

When the neuron is in the spiking regime, the system adheres to a different set of first-order linear differential equations. In the spiking system, the vector $\mathbf{b}^S(t)$ is now time-dependent, and both A^S and $\mathbf{b}^S(t)$ have one fewer dimension since the somatic voltage is entirely described by the spike shape $h(t)$. For the branch model, these quantities are given by

$$
A^S_{branch} =
\begin{bmatrix}
-1-\alpha_1 g_1 & 0 & \cdots & 0 \\
0 & -\gamma_2-\alpha_2 g_2 & \cdots & 0 \\
\vdots & \vdots & \ddots & \vdots \\
0 & 0 & \cdots & -\gamma_n-\alpha_n g_n
\end{bmatrix}
$$

$$
\text{and} \quad \mathbf{b}^S_{branch}(t) =
\begin{bmatrix}
\alpha_1 g_1 h(t) + I_1 \\
\alpha_2 g_2 h(t) + \gamma_2 \beta_2 + I_2 \\
\vdots \\
\alpha_n g_n h(t) + \gamma_n \beta_n + I_n
\end{bmatrix}. \tag{17}
$$

2.4.2. Chain model

Similarly, in the system with the chain topology, when the neuron is not spiking, the quantities A^{NS} and $\mathbf{b}^{NS}$ are given by

$$
A^{NS}_{chain}
$$
$$
=
\begin{bmatrix}
-1-\alpha_1 g_1-\alpha_1 g_2 & \alpha_1 g_2 & 0 & \cdots & \alpha_1 g_1 \\
\alpha_2 g_2 & -\gamma_2-\alpha_2 g_2-\alpha_2 g_3 & \alpha_2 g_3 & \cdots & 0 \\
0 & \alpha_3 g_3 & -\gamma_3-\alpha_3 g_3-\alpha_3 g_4 & \cdots & 0 \\
\vdots & \vdots & \vdots & \ddots & \vdots \\
g_1 & 0 & 0 & \cdots & -\gamma_S-g_1
\end{bmatrix}
$$

$$
\text{and} \quad \mathbf{b}^{NS}_{chain} =
\begin{bmatrix}
I_1 \\
\gamma_2 \beta_2 + I_2 \\
\vdots \\
\gamma_S \beta_S + I_S
\end{bmatrix}. \tag{18}
$$

When the neuron is in the spiking regime, the quantities $\mathbf{b}^S(t)$ and A^S are given by

$$
A^S_{chain}
$$
$$
=
\begin{bmatrix}
-1-\alpha_1 g_1-\alpha_1 g_2 & \alpha_1 g_2 & 0 & \cdots & 0 \\
\alpha_2 g_2 & -\gamma_2-\alpha_2 g_2 & \alpha_2 g_3 & \cdots & 0 \\
0 & \alpha_3 g_3 & -\gamma_3-\alpha_3 g_3 & \cdots & 0 \\
\vdots & \vdots & \vdots & \ddots & \vdots \\
0 & 0 & 0 & \cdots & -\gamma_n-\alpha_n g_n
\end{bmatrix}
$$

$$
\text{and} \quad \mathbf{b}^S_{chain}(t) =
\begin{bmatrix}
\alpha_1 g_1 h(t) + I_1 \\
\gamma_2 \beta_2 + I_2 \\
\vdots \\
\gamma_n \beta_n + I_n
\end{bmatrix}. \tag{19}
$$

2.5. Input conductance

Since we seek to explore how the topology of the dendritic tree affects the firing dynamics of the multi-compartment LIF neuron, we need to control for the change in current flow between the soma and dendritic tree caused by the addition of dendritic compartments. Input conductance is a measure of the influence of the dendritic tree on the soma [8]. In order to isolate and more clearly examine the effects of dendritic topology, we require a method of computing and controlling for the input conductance in our multi-compartment LIF neuron, which we describe here.

We define *normalized input resistivity* as the change in the non-spiking somatic steady-state voltage V_S^{ss} in response to the presence of a somatic input current I_S. More precisely,

$$
G^{-1} = \frac{V_S^{ss} - V_S^{ss}\big|_{I_S=0}}{I_S},
$$

where G is the input conductance. Since $\mathbf{V}^{ss} = -(A^{NS})^{-1}\mathbf{b}^{NS}$ (see Eq. (14)), we have:

$$
\begin{aligned}
G^{-1} &= -\left[(A^{NS})^{-1}\frac{(\mathbf{b}^{NS}-\mathbf{b}^{NS}|_{I_S=0})}{I_S}\right]_{n+1} \\
&= -[(A^{NS})^{-1}]_{\{n+1,n+1\}},
\end{aligned} \tag{20}
$$

since the matrix-vector product selects the last column of the matrix $(A_{NS})^{-1}$. Therefore, G is the inverse of the element at $(n+1, n+1)$ of $-(A^{NS})^{-1}$, which is a function of α_i, g_i, and γ_i. When all $\beta_i = 0$ and dendritic injected currents $I_i = 0$, then the somatic component of the input conductance is equivalent to the threshold current for monostable firing. Using Cramer's rule and the fact that the matrix A^S is equivalent to A^{NS} with the last row and column removed, we can write the input conductance equivalently as:

$$
G = -\frac{\det(A^{NS})}{\det(A^S)}. \tag{21}
$$

Using this expression, if the determinant in the numerator is expanded as a sum of minors, we notice that the input conductance is linear in γ_S, or any other term that appears in the diagonal element in A^{NS} but not in A^S. Applying the definition to the two-compartment model, we recover the expression from [6] (Eq. (5.8))

$$
G = \frac{g_1}{\alpha_1 g_1 + 1} + \gamma_S. \tag{22}
$$

For the branch model with n dendrites, the input conductance is:

$$
-G^{-1} = (A^{NS})^{-1}_{\{n,n\}} = \left(-\gamma_S - \sum_{i=1}^{n} g_i + \sum_{i=1}^{n}\frac{\alpha_i g_i^2}{\gamma_i + \alpha_i g_i}\right)^{-1},
$$

$$
G = \gamma_S + \sum_{i=1}^{n}\frac{g_i \gamma_i}{\gamma_i + \alpha_i g_i}, \tag{23}
$$

which is computed using block inversion of A^{NS}. For the chain model with two dendrites, the input conductance is:

$$
G = \frac{g_1(\gamma_2 + \alpha_2 g_2 + \alpha_1 g_2 \gamma_2)}{\gamma_2 + \alpha_2 g_2 + \alpha_1 g_2 \gamma_2 + \alpha_1 g_1(\gamma_2 + \alpha_2 g_2)} + \gamma_S. \tag{24}
$$

When comparing two different dendritic topologies, one way to isolate the effect of topology on the firing dynamics of the system is to require that the input conductance is same for both topologies, i.e., $G = \tilde{G}$. Thus, for a given value of a parameter x, we can compute $G(x)$, and then solve for the value of $\tilde{x}$ such that $G(x) = \tilde{G}(\tilde{x})$. For example, suppose we wish to study the effect of changing g_1 in both the two-compartment and the three-compartment branch model. Setting the input conductances to be equal gives the expression:

$$\frac{g_1}{\alpha_1 g_1 + 1} + \gamma_S = \frac{g_2 \gamma_2}{\gamma_2 + \alpha_2 g_2} + \frac{\tilde{g}_1}{\alpha_1 \tilde{g}_1 + 1} + \gamma_S.$$

Solving for $\tilde{g}_1$ yields

$$\tilde{g}_1 = g_1 - \frac{g_2 \gamma_2 (\alpha_1 g_1 + 1)^2}{g_1 g_2 \gamma_2 \alpha_1^2 + g_2 \gamma_2 \alpha_1 + \gamma_2 + a_2 g_2}.$$

Thus, using the above equation for $\tilde{g}_1$ allows the two-compartment and the three-compartment branch model to have the *same* input conductance as g_1 is varied. For higher-dimensional comparisons, this can be difficult to find analytically, and so a numerical procedure, such as a root-finder, can be used to solve $G(x) = \tilde{G}(\tilde{x})$ for $\tilde{x}$, for every value of x requested. As in this example, the relationship can be highly non-linear. We show in Section A.3 that the input conductance is monotonically increasing with respect to any biophysical parameter: α_i, g_i, and γ_i. In addition, for a fixed set of parameters, the input conductance increases monotonically with the number of dendrites. This relationship guarantees that there is at most one solution $\tilde{x}$ such that $G(x) = \tilde{G}(\tilde{x})$.

2.6. Return map construction

In this section, we derive an n-dimensional return map that takes the state of the neuron at the end of the jth spike to the state of the neuron at the end of the $(j + 1)$st spike or to the quiescent steady state. This n-dimensional map completely captures the firing dynamics of the $n + 1$-dimensional multi-compartment LIF model. Constructing the return map requires solving both the non-spiking and spiking systems to determine the state of the neuron after the next spike. These solutions can easily be obtained owing to the linearity of both the non-spiking and spiking systems. In effect, the map becomes a matrix update which can be implemented efficiently and applied to complex high-dimensional dendritic configurations.

2.6.1. Spiking solution

Assume that the system is at the beginning of the jth spike so that $t = t_s^j$. In this case, the somatic voltage is determined by the function $h(t)$ while the voltages of dendritic compartments are governed by (15). We assume that the voltage of dendritic compartment i is initially at some potential V_i^j. That is, we solve system (15) with the initial condition $\mathbf{V}(t_s^j) = \mathbf{V}^j \equiv [V_1^j, \ldots, V_n^j]^T$. To compute the solution to the spiking system, we first diagonalize the matrix $A^S = S^S \Lambda^S (S^S)^{-1}$ where Λ^S is the diagonal matrix containing the eigenvalues of A^S, and S^S is the matrix with corresponding eigenvectors in each column. The spiking solution is then given by

$$\mathbf{V}^S(t) = S^S \exp\{\Lambda^S(t - t_s^j)\}$$
$$\times \left((S^S)^{-1} \mathbf{V}^j + \int_0^{t - t_s^j} \exp\{-\Lambda^S s\}(S^S)^{-1} \mathbf{b}^S(s)\, ds \right), \quad (25)$$

where $\exp\{\cdot\}$ is the matrix exponential. The above solution describes the evolution of the state of the neuron until the end of the jth spike (i.e., $t \in [t_s^j, t_s^j + T_a)$).

The spiking solution can also be expressed as a map that takes the membrane potentials of the dendritic compartments at the onset of the jth spike $\mathbf{V}^j$ to the dendritic potentials at the end of the jth spike $\mathbf{V}^{j+\frac{1}{2}} = [V_1^{j+\frac{1}{2}}, \ldots, V_n^{j+\frac{1}{2}}]$:

$$\Phi_S : \mathbf{V}^j \to \mathbf{V}^{j+\frac{1}{2}} = \mathbf{V}^S(t_s^j).$$

Thus, Φ_S is the linear map given by

$$\Phi_S(\mathbf{V}^j) = \Omega^S \mathbf{V}^j + K^S, \quad (26)$$

where

$$\Omega^S = S^S \exp\{\Lambda^S T_a\}(S^S)^{-1}$$
$$K^S = S^S \exp\{\Lambda^S T_a\}\left(\int_0^{T_a} \exp\{-\Lambda^S s\}(S^S)^{-1} \mathbf{b}^S(s) \right). \quad (27)$$

2.6.2. Non-spiking solution

At the end of the jth spike, the voltages of the dendritic compartments are given by $\mathbf{V}^{j+\frac{1}{2}}$ while the voltage of the somatic compartment is at its reset potential V_R. To obtain the voltage evolution during the time between the end of the jth spike and the onset of the $(j + 1)$st spike, we solve system (14) with the initial condition $\mathbf{V}(t_s^j + T_a) = [V_1^{j+\frac{1}{2}}, \ldots, V_n^{j+\frac{1}{2}}, V_R]^T$. Again, we first diagonalize the matrix $A^{NS} = S^{NS} \Lambda^{NS}(S^{NS})^{-1}$ where Λ^{NS} is the diagonal matrix containing the eigenvalues of A^{NS}, and S^{NS} is the matrix with corresponding eigenvectors in each column. The solution of system (14) is then given by

$$\mathbf{V}^{NS}(t) = (\mathbb{I} - W_j(t))\mathbf{V}^{ss} + W_j(t)\mathbf{V}(t_s^j + T_a), \quad (28)$$

where

$$W_j(t) = S^{NS} \exp\left\{\Lambda^{NS}(t - t_s^j - T_a)\right\}(S^{NS})^{-1}, \quad (29)$$

$\mathbb{I}$ is the $(n + 1) \times (n + 1)$ identity matrix, $\mathbf{V}^{ss} = -(A^{NS})^{-1}\mathbf{b}^{NS}$ is the steady-state solution of (14) and $\exp\{\cdot\}$ is again the matrix exponential. The above solution describes the evolution of the state of the neuron until the next spike is elicited (i.e., $t \in [t_s^j + T_a, t_s^{j+1})$). With biophysically-plausible values for the parameters, the eigenvalues are negative and real, and so as $t \to \infty$, $\exp\{\Lambda^{NS}t\}$ will approach the zero matrix. As a result, $\mathbf{V}^{NS}(t)$ will approach $\mathbf{V}^{ss}$. Whether or not the neuron reaches threshold and fires the $(j + 1)$st spike depends on the parameter values and the dendritic voltages at the end of the jth spike $\mathbf{V}^{j+\frac{1}{2}}$. More precisely, the neuron will fire the $(j + 1)$st spike if the somatic voltage reaches $V_{th} = 1$. This condition translates to the following transcendental equation [1]

$$V_S^{NS}(t_s^{j+1}) = V_S^{ss} + \left[W_j(t_s^{j+1})\right]_{\{n+1,n+1\}}\left(V_R - V_S^{ss}\right)$$
$$+ \sum_{i=1}^{n} \left[W_j(t_s^{j+1})\right]_{\{n+1,i\}}\left(V_i^{j+\frac{1}{2}} - V_i^{ss}\right) = 1, \quad (30)$$

having a finite positive solution for t_s^{j+1}. In the above equation, $[W_j(t_s^{j+1})]_{\{n+1,i\}}$ refers to the $(n + 1, i)$th element of the matrix $W_j(t_s^{j+1})$ (see Eq. (29)), and we have used the fact that the first n elements of the vector $\mathbf{V}(t_s^j + T_a)$ are equivalent to the vector $\mathbf{V}^{j+\frac{1}{2}}$. Recall again that the non-spiking system (14) has $n + 1$ dimensions with the $(n + 1)$st dimension being the dynamics for the somatic voltage. If a positive solution to (30) does not exist, the neuron evolves to the quiescent steady state without firing. As (30) is a transcendental equation, the smallest positive solution is approximated using a numerical root-finding method.

The non-spiking solution can be expressed as a map that takes the membrane potentials of the dendritic compartments at the end of the jth spike $\mathbf{V}^{j+\frac{1}{2}}$ to the membrane potentials of the dendritic compartments at the onset of the $(j + 1)$st spike $\mathbf{V}^{j+1} = [V_1^{j+1}, \ldots, V_n^{j+1}]$.

$$\Phi_{NS} : \mathbf{V}^{j+\frac{1}{2}} \to \mathbf{V}^{j+1} = \left[\mathbf{V}^{NS}(t_s^{j+1})\right]_{\{1:n\}},$$

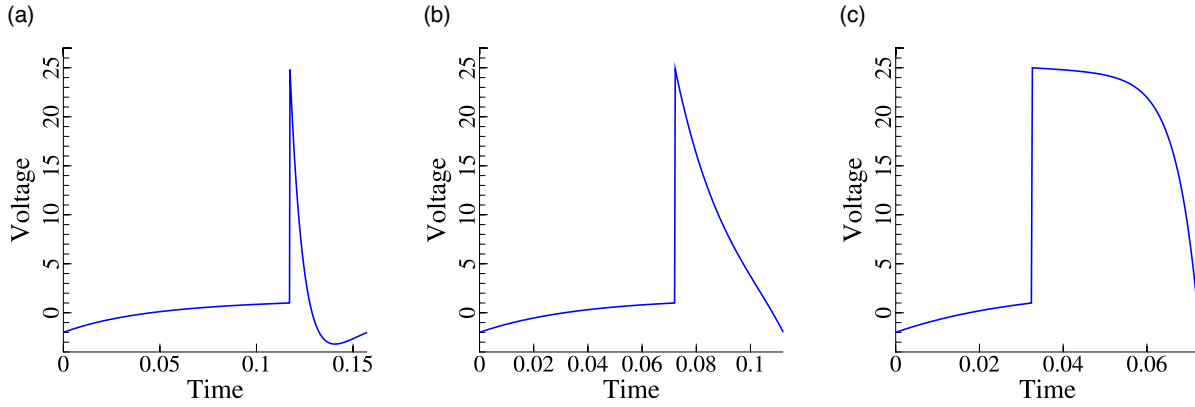[1] Note that this equation is simply the $(n + 1)$st component of (28) evaluated at $t = t_s^{j+1}$.

Fig. 1. Variety of spike shapes. Somatic voltage traces in the three-compartment branch model with spike shape parameters $p = 0.05$ for (a), $p = 0.55$ for (b), and $p = 0.90$ for (c). Note that the firing frequency increases with p, which we explore in later sections. The other parameters used to generate these figures were: $\alpha_1 = \alpha_2 = 5$, $g_1 = g_2 = 3$, $\beta_S = 1$, $\gamma_S = 16$, $V_R = -2$, $I_1 = I_2 = 0$, $I_S = 11$, and $T_a = 0.04$. The maximal potential of the spike was 25.

where $[\mathbf{V}^{NS}(t_s^{j+1})]_{\{1:n\}}$ denotes the first n elements of the $n + 1$ dimensional vector $\mathbf{V}^{NS}(t_s^{j+1})$. More precisely,

$$\Phi_{NS}(\mathbf{V}^{j+\frac{1}{2}}) = \begin{cases} \Omega_j^{NS}\mathbf{V}^{j+\frac{1}{2}} + K_j^{NS}, & \text{if a positive solution,} \\ & \text{to (30) exists} \\ [\mathbf{V}^{ss}]_{\{1:n\}}, & \text{otherwise,} \end{cases} \quad (31)$$

where

$$\Omega_j^{NS} = \left[W_j(t_s^{j+1}) \right]_{\{1:n,1:n\}}$$

$$K_j^{NS} = \left[\left(\mathbb{I} - W_j(t_s^{j+1}) \right) \mathbf{V}^{ss} \right]_{\{1:n\}} + V_R \sum_{i=1}^{n} \left[W_j(t_s^{j+1}) \right]_{\{i,n+1\}}. \quad (32)$$

2.6.3. The return map

Using the two maps we detailed in the previous sections, we can define a new map Φ which takes the voltages of the dendritic compartments at the time of the jth spike $\mathbf{V}^j$ to the voltages of the dendritic compartments at the time of the $(j + 1)$st spike $\mathbf{V}^{j+1}$ or the quiescent steady state $[\mathbf{V}^{ss}]_{\{1:n\}}$

$$\mathbf{V}^{j+1} = \Phi(\mathbf{V}^j) = \Phi_{NS} \circ \Phi_S(\mathbf{V}^j)$$
$$= \begin{cases} \Omega_j^{NS}[\Omega^S\mathbf{V}^j + K^S] + K_j^{NS}, & \text{if a positive solution} \\ & \text{to (30) exists,} \\ [\mathbf{V}^{ss}]_{\{1:n\}}, & \text{otherwise.} \end{cases} \quad (33)$$

By iterating this n-dimensional map, the dynamics of the full multi-compartment neuronal model can be assessed. Note, however, that even though (33) is linear, each iteration involves solving the transcendental Eq. (30) for t_s^j, in order to evaluate Ω_j^{NS} and K_j^{NS}. Fixed points of this map correspond to either periodic oscillations or quiescent behavior. While we would like to prove that the map is a contraction, the transcendental nature of Eq. (30) makes this difficult.

3. Results

We now examine the behavior of the multi-compartment LIF neuron by analyzing the map derived in the previous section. First, we describe the functional forms for the spike shape function $h(t)$ that we use in our analysis. We then determine the parameter values at which the time-independent "quiescent" steady-state ceases to exist and the parameter values at which stable periodic oscillations appear. Similar to [6], we find that the system can display bistability between periodic firing and quiescence. However, we find significant quantitative differences in the firing dynamics of the system depending upon the topology of the dendritic tree.

3.1. Spike shape

We describe the construction of the spike shape family and its parameterization in this section. The goal is to attain a one-parameter description of the spike shape that captures a large variety of waveforms. We found that a sum of two exponentials would provide the expressive freedom to do so:

$$h_p(t) = -\frac{p_b}{p_a - p_d} \exp\left\{\frac{p_d t}{T_a}\right\} + \left(H + \frac{p_b}{p_a - p_d}\right) \exp\left\{\frac{p_a t}{T_a}\right\}, \quad (34)$$

where $p_a = 5.9022p - 5.3478$ and $p_b = -80 \exp\{-7.377p\} - 2(10^{-5})$. The value of p_d is solved for numerically with the constraints $h(T_a) = V_R$ and $h(0) = H$. To solve for p_d, we used Dekker's method [19] to find the root of the expression $h(T_a) - V_R$. For values of p between 0 and 1, we observe that the first exponential is asymptotically dominant and a unique root exists. Also note that time is scaled by the spike duration T_a. This is to ensure that any change in T_a will result in a horizontal linear scaling of the spike shape. The constants used in the expressions for p_a and p_b were set such that the resulting spike shape exhibited afterhyperpolarization and a diverse range of waveforms. The shape of the spike can be controlled with the parameter p, where $p = 0$ has a much thinner spike with a large subsequent region of afterhyperpolarization. For $p \approx 0.6$, the spike has a shape similar to a line, connecting $h(0) = H$ to $h(T_a) = V_R$. Finally, when $p = 1$, the spike shape becomes much larger, curving upward and then falling sharply back down to $h(T_a) = V_R$. The voltage traces in Fig. 1 show the effect of varying p on the shape of the resulting spike. This parameterization allows us to continuously explore the effect of a changing spike shape with and without afterhyperpolarization, including a very wide spike shape that adds considerable current to the system.

3.2. Return map analysis

The return map enables us to explore the firing dynamics of the full multi-compartment LIF model. We characterize the firing state of the neuron into three classes: the quiescent steady state, monostable periodic firing, and a bistable state where periodic firing and the quiescent state co-exist. In the quiescent state, no matter what the initial membrane potentials are, the neuron will eventually cease firing and approach a time independent steady state as time goes to infinity. Similarly, in the monostable firing state, the neuron will continue spiking periodically, regardless of the initial conditions. The monostable firing state can be reached by increasing the applied current to the soma I_S so that the steady state somatic voltage is above threshold, i.e., $V_S^{ss} > V_{th} = 1$. This threshold current I_{th} corresponds the current at which the $(n + 1)$st component (the somatic element)
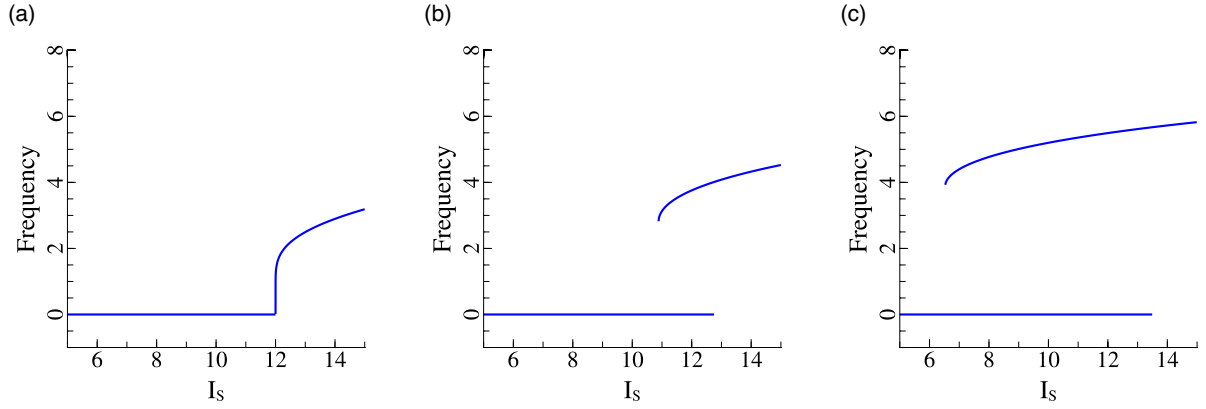
Fig. 2. Firing rate vs. input. Simulated normalized firing frequency plotted against input somatic current I_S of: (a) the one-compartment LIF model, (b) two-compartment model, and (c) three-compartment branch model where $\alpha_1 = \alpha_2 = 1$, $g_1 = g_2 = 3$, $\gamma_2 = 1$, $\gamma_S = 12$, $\beta_2 = \beta_S = 0$, $I_1 = I_2 = 0$, $V_R = -2$, $T_a = 0.1$, and a spike with maximal potential 80 with shape parameter $p = 0.05$.

of $\mathbf{V}^{ss} = -(A^{NS})^{-1}\mathbf{b}^{NS}$ is equal to the threshold potential $V_{th} = 1$:

$$V_S^{ss} = -[(A^{NS})^{-1} \cdot \mathbf{b}^{NS}]_{n+1} = -[(A^{NS})^{-1}]_{\{n+1,n+1\}}b_{n+1}(I_S)$$

$$- \sum_{i=1}^{n}[(A^{NS})^{-1}]_{\{n+1,i\}}b_i = 1, \qquad (35)$$

where $[(A^{NS})^{-1}]_{\{n+1,i\}}$ is the element of the matrix $(A^{NS})^{-1}$ in the row $n+1$ and column i and b_i is the ith element of the vector $\mathbf{b}^{NS}$. Inverting the function $b_{n+1}(I_S)$ allows us to solve for this threshold current

$$I_{th} = b_{n+1}^{-1}\left(\frac{V_{th} + \sum_{i=1}^{n}[(A^{NS})^{-1}]_{\{n+1,i\}}b_i}{[A^{NS}]_{\{n+1,n+1\}}}\right). \qquad (36)$$

Note that the term $b_{n+1}(I_S)$ is typically a linear function of I_S and thus its inverse $b_{n+1}^{-1}(\cdot)$ can easily be computed. For example, the threshold somatic current for the branch model with two dendrites is given by

$$I_{th} = \frac{V_{th}B}{(\alpha_1 g_1 + 1)(\gamma_2 + \alpha_2 g_2)} - \frac{I_1 g_1}{\alpha_1 g_1 + 1}$$

$$- \frac{g_2(I_2 + \beta_2 \gamma_2)}{\gamma_2 + \alpha_2 g_2} - \beta_S \gamma_S, \qquad (37)$$

where $B = g_1\gamma_2 + g_2\gamma_2 + \gamma_2\gamma_S + \alpha_2 g_1 g_2 + \alpha_2 g_2\gamma_S + \alpha_1 g_1 g_2\gamma_2 + \alpha_1 g_1\gamma_2\gamma_S + \alpha_1\alpha_2 g_1 g_2\gamma_S$. We note that this threshold current is independent of the spike shape. Whenever $I_S > I_{th}$, then the system is guaranteed to be in the monostable firing regime.

For the single compartment LIF model, the system can only be in either the quiescent state or the monostable firing state depending on the value of I_S as shown in Fig. 2(a). However, for the multi-compartment LIF neuron and for certain settings of the parameters, there exists a range of values of $I_S < I_{th}$ where the system can be in either the quiescent state or the periodic firing state depending upon the initial conditions. This bistability is illustrated in Fig. 2(b) for the two compartment model and in Fig. 2(c) for the three compartment branch model. In previous work [6], it was shown that bistability in the two-compartment model resulted from a somato-dendritic *ping-pong effect*, where the dendritic compartment becomes sufficiently depolarized from the previous somatic spike that the resulting flow of current back into the soma after the spike causes the soma to reach threshold and fire a subsequent spike. Although the mechanism for bistability is the same in the multi-compartment LIF model, the topology of the dendritic tree can have significant quantitative effects on the size of the bistable region in parameter space. For example, in comparing Fig. 2(b) and (c), one can see that the addition of the second dendritic compartment causes bistability to persist for a larger range of values for I_S. Fig. 3 plots an example voltage trace for the three compartment branch model in the bistable regime. The
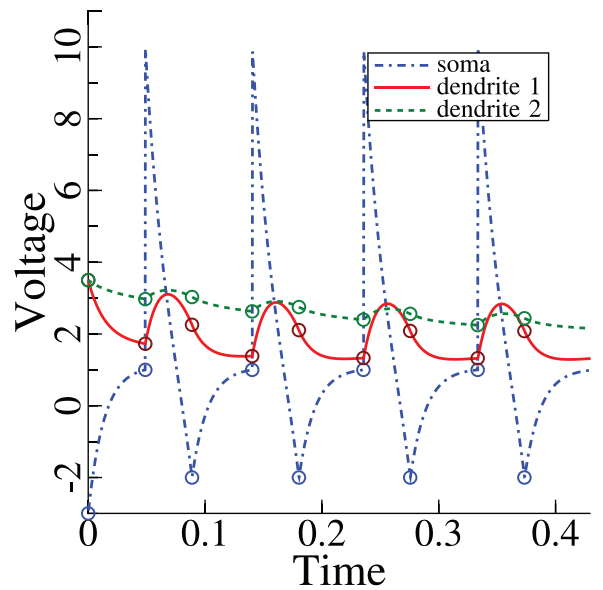

Fig. 3. Three compartment voltage trace. A voltage trace of the three-compartment branch model where $\alpha_1 = 5$, $\alpha_2 = 1$, $g_1 = g_2 = 4$, $\gamma_2 = 1$, $\gamma_S = 64$, $\beta_2 = 5$, $\beta_S = 1$, $I_1 = 10$, $I_2 = 0$, $I_S = -5$, $V_R = -2$, $T_a = 0.04$, and a spike with maximal potential 10 with shape parameter $p = 0.55$. The initial conditions are $V_1 = V_2 = 3.5$ and $V_S = -3$. The curves were generated using order-4 Runge–Kutta to simulate the system. The circles indicate the values of the solution as predicted by the non-spiking and spiking portions of return map.

ping-pong effect can be seen as the dendritic potentials remain highly depolarized at the end of the somatic spike.

To better understand how this bistability emerges in higher dimensional systems, we visualize the discrete return map (33) with two dendritic compartments in a "phase plane". We put phase plane in quotes as the system is discrete and standard phase plane analysis is applied to continuous dynamical systems. To generate the vector field for the map, we use

$$\begin{bmatrix} V_1^{j+1} - V_1^j \\ V_2^{j+1} - V_2^j \end{bmatrix} = \begin{bmatrix} \Phi_1(V_1^j, V_2^j) - V_1^j \\ \Phi_2(V_1^j, V_2^j) - V_2^j \end{bmatrix}$$

which represents the total change in the V_1 and V_2 components over one iteration of the map. Thus, the right-hand side of the above equation can be viewed as a vector field for the reduced system which is plotted in Fig. 4 for the three compartment branch model with three different values of I_S. More precisely, the vector field in Fig. 4 visualizes the direction and relative magnitude of the difference between the next and the current iteration of the return map, over
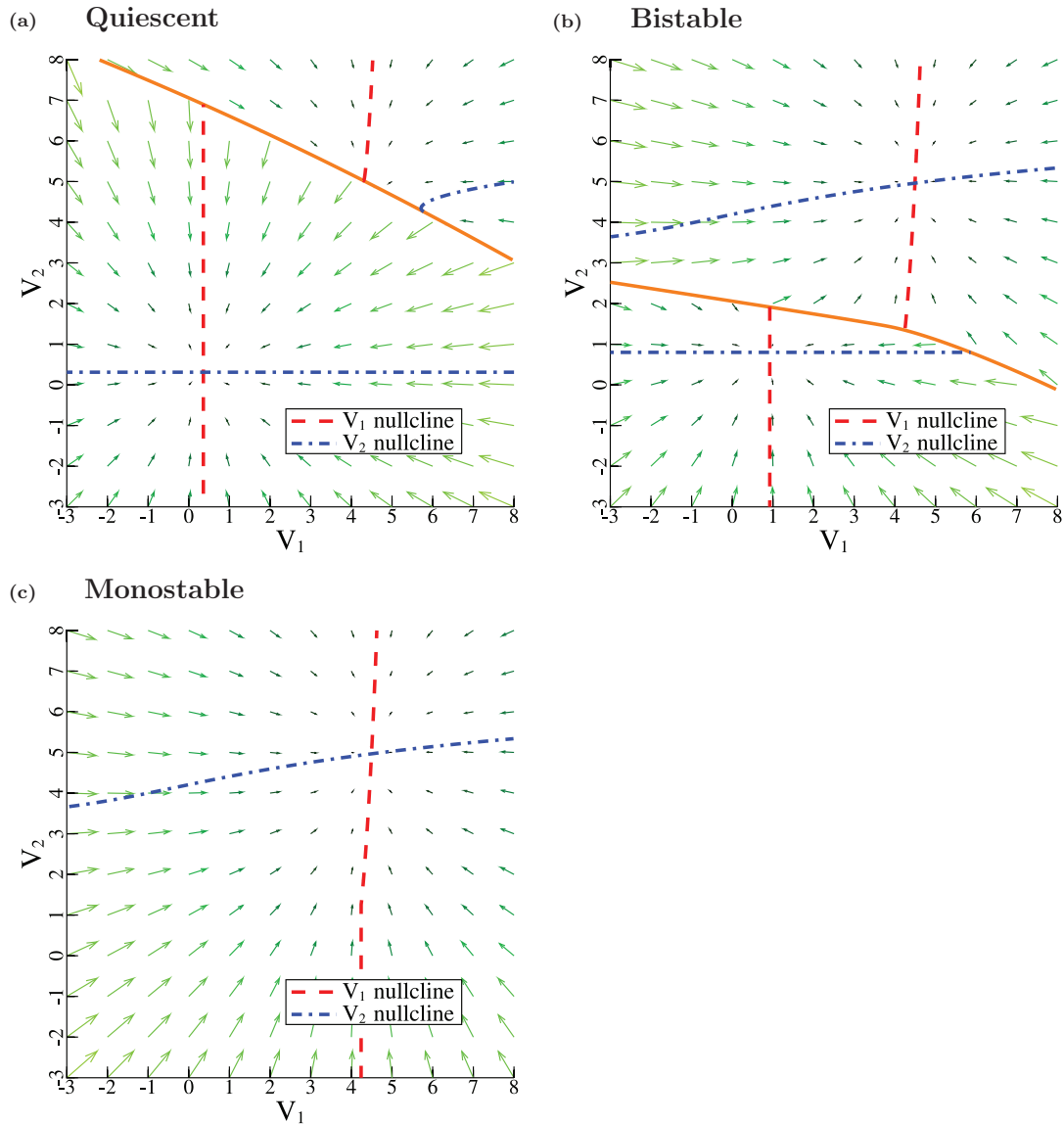
Fig. 4. Return map. A vector field representation of the return map where the arrows indicate the direction and relative magnitude of the difference between the next iteration and current iteration of the map. Here the three-compartment branch model is used, and the other parameters: $\alpha_1 = 3$, $\alpha_2 = 1$, $g_1 = g_2 = 4$, $\beta_2 = \beta_S = 0$, $\gamma_2 = 1$, $\gamma_S = 12$, $I_1 = I_2 = 0$, $I_S = 5.1$ (top-left), $I_S = 13.1$ (top-right), and $I_S = 13.2$ (bottom-left). As the current is increased, we see the neuron switches from the quiescent state (top-left) into a bistable regime (top-right), and finally, monostability (bottom-left). The spike duration is $T_a = 0.1$, the spike height is $H = 80$, and shape parameter is $p = 0.05$. The solid curve separates the spiking region from the non-spiking region.

the possible values of the current iteration. The values of V_2 where $\Phi_1(V_1, V_2) - V_1 = 0$ and V_1 where $\Phi_2(V_1, V_2) - V_2 = 0$ respectively represent the V_1 and V_2 nullclines and are plotted as the dashed and dashed-dotted lines. The solid line in the plots separates the region where the neuron does not spike and the region where the neuron spikes at least once (i.e., a finite positive solution to (30) exists). Fig. 4(a) plots the phase plane when the system is in the quiescent state: the only stable steady state is (V_1^{ss}, V_2^{ss}), at the intersection of the V_1 and V_2 nullclines. Bistability is shown in Fig. 4(b) as a second stable steady-state corresponding to the intersection of the nullclines in the upper right quadrant now coexists with the quiescent state. Lastly, Fig. 4(c) shows the monostable firing regime where the quiescent state no longer exists.

Next, we explore how the spike shape we detailed in the previous section affects the size of the bistable region in the two compartment model. Fig. 5(a) plots a two-parameter bifurcation diagram of the injected somatic current I_S versus the spike shape parameter p. Above the solid line (which corresponds to $I_s = I_{th}$, the system is always in the monostable firing regime. However, as the spike shape is varied,

one can see that for values of $I_S < I_{th}$ the system displays bistability. This shows that wider spike shapes readily promote bistability. However, as Fig. 5(b) shows, wider spike shapes also cause large changes in the firing frequency of the system. Thus, in order to remove the effect of spike shape on the firing frequency, we focus our subsequent exploration on the system with the spike shape $p = 0.05$. This thinner spike is more similar to spike shapes observed in recordings from biological neurons, and is in a range where bistability is not readily observed (see Fig. 5(a)) and where the firing frequency does not vary greatly for values of p near 0.05. Thus, any bistable behavior we observe will be due to the parameters of the system as well as the dendritic tree topology.

3.3. Effects of dendritic tree properties on the firing dynamics of the multi-compartment LIF model

As the system has a very large number of parameters, we focus on key insights obtained by varying a subset of the parameters in the model. Specifically, we examine: α_1, the ratio of the surface area of
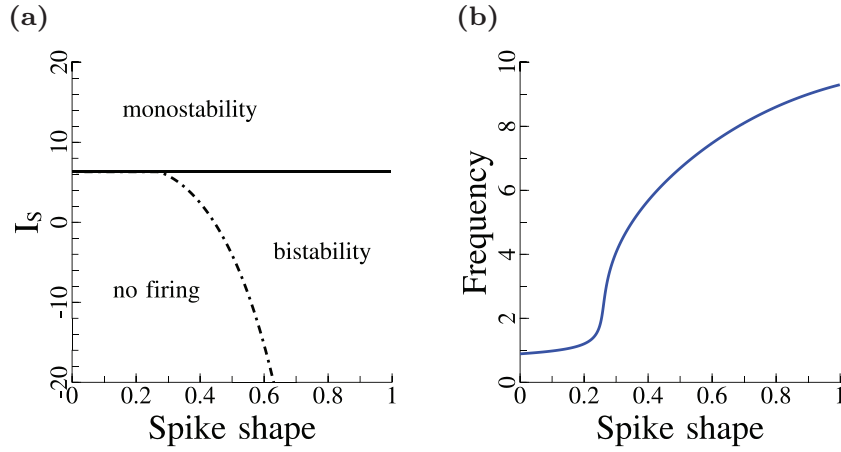
(a)

(b)

Fig. 5. Effect of spike shape parameter. Left: A two-parameter bifurcation diagram exploring the effect of the spike shape parameter on the stability of the two-compartment model. The solid line is $I_{S,th}$, the threshold injected current such that any higher current will result in the neuron always spiking periodically, as described by Eq. (36). Right: A plot of normalized spike frequency as a function of the spike shape parameter p where I_S is fixed to 6.4. The parameters used to generate this figure were: $\alpha_1 = 3$, $g_1 = 5$, $\beta_S = 0$, $\gamma_S = 6$, and $I_1 = 0$. The maximal potential of the spike was set to $H = 80$. The spike duration T_a is fixed to 0.1.
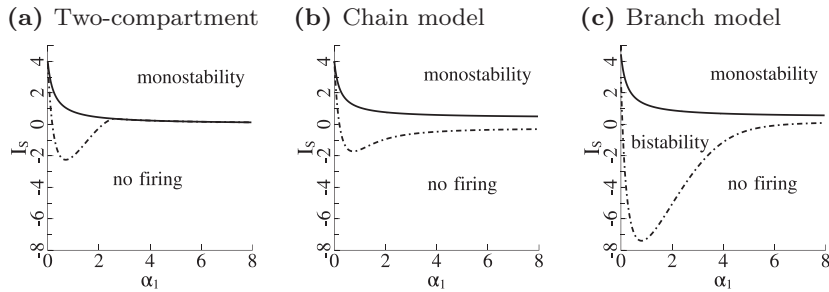
(a) Two-compartment   **(b)** Chain model   **(c)** Branch model

Fig. 6. Effect of α_1 in two and three compartments. Two-parameter bifurcation diagrams showing differences in stability with varying α_1, the ratio of the somatic area to the surface area of the first compartment, between the two-compartment model, the three-compartment chain model, and the three-compartment branch model, respectively, from left to right. The dashed-dotted line denotes the minimum injected somatic current needed to sustain oscillations, and any smaller value will result in the neuron becoming quiescent. The parameters used to produce these figures are $\alpha_2 = 2$, $g_1 = g_2 = 4$, $\gamma_2 = 1$, $\gamma_S = 12$, $\beta_2 = 0$, $\beta_S = 1$, $I_1 = I_2 = 0$, $V_R = -2$, $T_a = 0.1$, spike shape $p = 0.05$, and maximal spike potential $H = 80$.

the soma to the area of the first dendrite, g_1, the normalized coupling conductance between the soma and the first dendrite, and the spike duration T_a, which influences the area of spike, and therefore, the current to and from the dendrites. Since the first dendrite is always directly connected to the soma in our exploration, variation of its parameters will have the greatest effect on the firing dynamics of the system. For this reason, we focus on varying the biophysical parameters of the first dendrite.

3.3.1. Addition of a dendritic compartment

We first compare the firing dynamics of the two-compartment model, the three-compartment branch model, and the three-compartment chain model. In the following figures, we examine the effect of varying each biophysical parameter. No parameter in the model is adjusted to maintain a constant input conductance.

Fig. 6 presents a set of two-parameter bifurcation diagrams of the injected somatic current I_S versus α_1, the ratio of the somatic surface area to that of the first compartment. Notice that the bifurcation diagram for the two-compartment model (left) has a bistable region that ends at some finite value of α_1. This is in contrast with both three-compartment models (middle and right), where the bistable region extends out further. In fact, this behavior is not possible in the two-compartment model, since in the limit $\alpha_1 \to \infty$, the size and influence of the dendritic compartment goes to zero. In fact, in the branch model, as $\alpha_1 \to \infty$, the system is an effective two-compartment model where the parameters of the dendrite are equivalent to the parameters of the second dendrite in the original neuron. In the chain model, as $\alpha_1 \to \infty$, the system becomes an effective

two-compartment model with parameter $g^{new} = \frac{g_1 g_2}{g_1 + g_2}$. In all of the diagrams, we see that there exists a value of α_1 such that the width of the bistable region is maximal. Since the input conductance is not held constant in these experiments, the size of the bistable region increases with the addition of a dendritic compartment. This is particularly pronounced in the three-compartment branch model, where the input conductance is highest. We show in Section A.4 that neurons with flatter and more highly branched dendritic architectures have larger input conductances.

In Fig. 7, there are a set of two-parameter bifurcation diagrams of the injected somatic current I_S versus g_1, the normalized coupling conductance parameter of the electrical coupling between the soma and the first dendrite. As with varying the ratio of the somatic surface area to that of the first compartment α_1, we see similar differences in behavior between the three models when we vary the coupling conductance g_1. The addition of a dendrite increases the size of the bistable region, as evident in both the middle and right images (three-compartment chain and branch models), but especially so in the branch model since input conductance is maximal with respect to topology. Note, however, that in the chain model, the bistable region persists for much larger values of g_1 than in the branch model. In our simulations, we found points in the parameter space where the size of the bistable region does not increase with the addition of dendrites, such as with wider spike shapes (results not shown). This suggests that although input conductance plays a large role in the firing dynamics of the neuron, it is not the only factor that can influence bistability. "Longer" dendritic structures seem to extend the range of parameter values in which bistability is observed. Finally, we
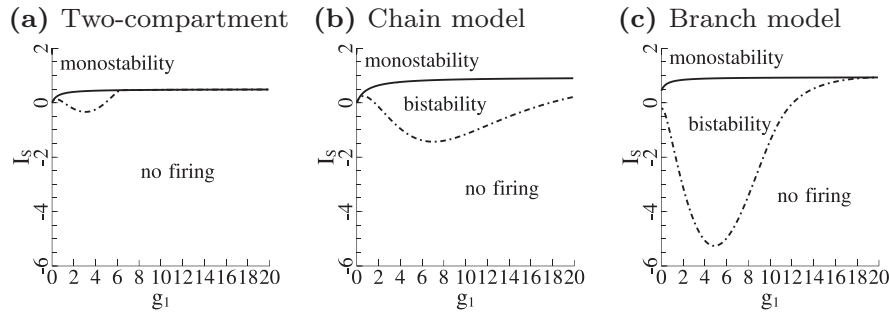
(a) Two-compartment   **(b)** Chain model   **(c)** Branch model

Fig. 7. Effect of g_1 in two and three compartments. Two-parameter bifurcation diagrams showing differences in stability with varying g_1, the normalized conductance parameter of the coupling between the soma and first compartment, between the two-compartment model, the three-compartment chain model, and the three-compartment branch model, respectively, from left to right. The parameters used to produce these figures are $\alpha_1 = \alpha_2 = 2$, $g_2 = 4$, $\gamma_2 = 1$, $\gamma_S = 12$, $\beta_2 = 0$, $\beta_S = 1$, $I_1 = I_2 = 0$, $V_R = -2$, $T_a = 0.1$, spike shape $p = 0.05$, and maximal spike potential $H = 80$.

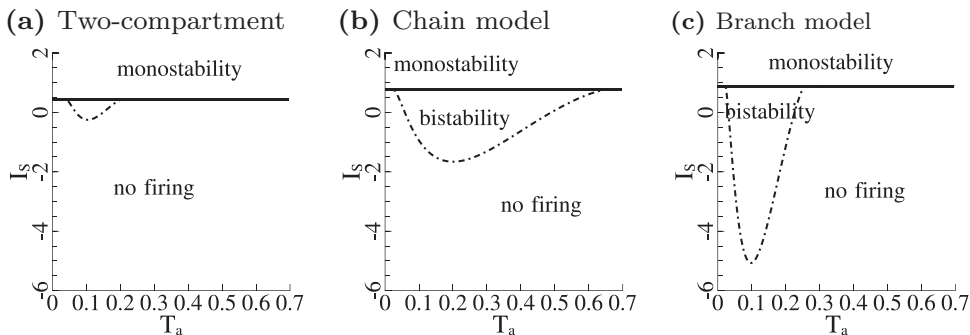**(a)** Two-compartment   **(b)** Chain model   **(c)** Branch model

Fig. 8. Effect of spike duration in two and three compartments. Two-parameter bifurcation diagrams showing differences in stability with varying the spike duration T_a between the two-compartment model (a), the three-compartment chain model (b), and the three-compartment branch model (c). The parameters used to produce these figures are $\alpha_1 = \alpha_2 = 2$, $g_1 = g_2 = 4$, $\gamma_2 = 1$, $\gamma_S = 12$, $\beta_2 = 0$, $\beta_S = 1$, $I_1 = I_2 = 0$, $V_R = -2$, spike shape $p = 0.05$, and maximal spike potential $H = 80$.

note that when $g_1 = 0$ in the three-compartment branch neuron, the system reduces to the two-compartment model where $g_1 = 4$. Unlike in the two-compartment model, bistability does not disappear in the branch model when $g_1 = 0$.

Fig. 8 presents two-parameter bifurcation diagrams of the applied somatic current I_S versus the spike duration T_a. Comparing the middle and right bifurcation diagrams, we again observe that the longer dendritic topology exhibits a wider range of spike durations for which the neuron can be bistable. In contrast, the bistable region of the branchier dendritic topology is thinner and much taller. This again supports the fact that input conductance does not fully explain the size of the bistable region. In this case, dendritic topology has a clear effect. We see in all of the dendritic topologies and spike shapes we tested in our simulations, there is a value of the spike duration at which the width of the bistable region is maximal. If the spike duration is too small, there is no value of the injected somatic current for which the neuron is bistable, since there is not enough time for current to flow into the dendrites and facilitate the ping-pong effect. If the spike duration is too long, a longer period of time is required for the somatic voltage to return to the reset voltage, which enables the dendrites to leak current to the soma before the spiking regime ends. This optimal spike duration varies with spike shape. Thinner spike shapes have a smaller optimal spike duration whereas wider spike shapes have a longer optimal duration (results not shown). As with the previous results, we see that the size of the bistable region in the three-compartment branch model (right) is much larger than that of the two-compartment model (left) and the three-compartment chain model (middle). Bistability is persistently encouraged when the spike height is increased (results not shown).

3.3.2. Addition of dendritic compartment with input conductance held constant

Here, we again compare the firing dynamics of the two-compartment model, the three-compartment branch model, and the
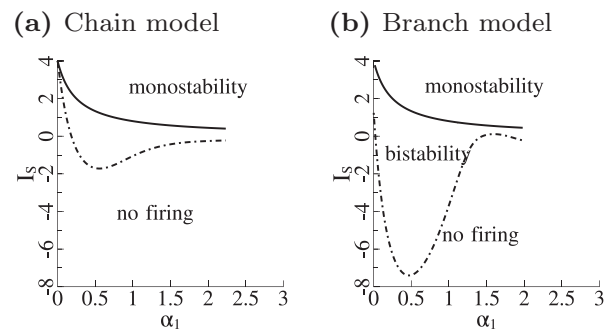
(a) Chain model   **(b)** Branch model

Fig. 9. Effect of α_1 with normalized input conductance. Two-parameter bifurcation diagrams showing differences in stability with varying α_1, the ratio of the somatic area to the surface area of the first compartment, between the three-compartment chain model and branch model, respectively, from left to right. The dashed-dotted line denotes the minimum injected somatic current needed to sustain oscillations, and any smaller value will result in the neuron becoming quiescent. The parameters used to produce these figures are $\alpha_2 = 2$, $g_1 = g_2 = 4$, $\gamma_2 = 1$, $\gamma_S = 12$, $\beta_2 = 0$, $\beta_S = 1$, $I_1 = I_2 = 0$, $V_R = -2$, $T_a = 0.1$, spike shape $p = 0.05$, and maximal spike potential $H = 80$.

three-compartment chain model. However, in these diagrams, we control for differences in input conductance between the different models using the method outlined in Section 2.5. For example, in Fig. 9, there are two-parameter bifurcation diagrams of the input somatic current I_S versus α_1, the ratio of the somatic surface area to that of the first dendrite. For a particular value of α_1 in the two-compartment model, the input conductance $G(\alpha_1)$ is computed. To maintain the same input conductance in the corresponding three-compartment model, we numerically compute the value of $\tilde{\alpha}_1$ such that the resulting input conductance in the three-compartment model $\tilde{G}(\tilde{\alpha}_1)$ is equivalent to the input conductance of the two-compartment model $G(\alpha_1)$. For brevity, we only report the results for α_1, since many of the results for other parameters are consistent with
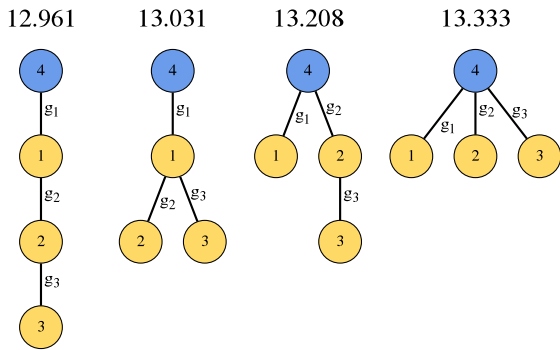
Fig. 10. Dendritic topologies in four compartments. A plot of the dendritic topologies of the four-compartment neuron with labeled connections and compartments. This is the order in which the two-parameter bifurcation diagrams are presented in Fig. 11. The value above each topology denotes the input conductance for the parameters: $\alpha_i = 2$, $g_i = 4$, $I_i = 0$ for all i; $\beta_i = 0$, $\gamma_i = 1$ for all dendrites i and $\beta_S = 1$, $\gamma_S = 12$; $V_R = -2$, spike shape parameter $p = 0.05$, spike duration $T_a = 0.1$, with maximal spike potential $H = 80$.

those presented in Fig. 9. Note that the input conductance is constant with respect to the spike duration T_a, spike shape p, maximum spike potential H, injected current I_i, and normalized leakage reversal potential β_i, for all compartments i.

In Fig. 9, there are regions in the bifurcation diagrams that are undefined. This is due to the fact that the equation $G(\alpha_1) = \tilde{G}(\tilde{\alpha}_1)$ may not have a feasible solution, using the notation from Section 2.5. More specifically, the numerically computed value of $\tilde{\alpha}_1$ that satisfies $G(\alpha_1) = \tilde{G}(\tilde{\alpha}_1)$ goes to infinity at some finite asymptote. This reveals a previously unseen behavior which is more evident in the right bifurcation diagram. For neurons with three or more compartments, as the value of α_1 is increased, the width of the bistable region first grows and reaches a maximum width. As α_1 is further increased, the bistable region shrinks to a minimum width and then begins to grow again. This behavior is only observed for the thinnest spike shapes $p = 0.05$, and is directly a result of the spike shape. For small values of α_1, the dendrite does not play an influential role in the spiking dynamics of the neuron. But as the parameter value increases, the dendrite more readily loses current due to the afterhyperpolarization in the spike shape, depressing the ping-pong effect. For sufficiently large values of the parameter, the dendrite begins to more closely track the voltage of its immediately connected neighbor compartments. Thus, the current provided by the initial upward spike is quickly absorbed by the dendrite, allowing the dendrite to contribute to bistability once again. The dendrite is closer to the soma in branchier topologies, which is why the behavior is typically more pronounced in those dendritic topologies. This suggests that input conductance does not solely determine the quantitative bifurcation structure of the neuron. Dendritic morphology plays an influential role.

3.3.3. Dendrite count held constant

In this subsection, we explore the effect of dendritic topology of the four-compartment neuron on firing dynamics. Only the topology

of the neuron is varied, without adjusting the input conductance. The explored topologies are depicted in Fig. 10, with labeled compartments and connections.

In Fig. 11, we present two-parameter bifurcation diagrams of the injected somatic current versus g_1. We observe in most of the bifurcation diagrams that the neurons with greater input conductance have larger bistable regions. However, as we saw in the three-compartment model, this is not always the case. In the above figure, there are portions of the bistable region that are clearly smaller in the branchier topologies with higher input conductance. Interestingly, we observed in our simulations that this effect is not apparent with wider spike shapes (results not shown). The maximum width of the bistable region, however, does seem to correspond strongly with the input conductance of the topology.

3.4. Firing dynamics in more complex dendritic topologies

To show that our method is easily extendable to more complex dendritic topologies, we generate a number of bifurcation diagrams testing various biophysical parameters for the dendritic topology shown in Fig. 12(a). In Fig. 12(b), the normalized conductance of the connection between the soma and the first dendrite g_1 is varied, and the overall shape is very similar to those in the earlier g_1 bifurcation diagrams. For instance, note that bistability is present for any value of g_1. Fig. 12(c) was generated by varying α_1, which is the ratio of the surface area of the soma and the area of the first dendrite. The dashed line reaches the asymptote quickly, which is similar to the behavior observed in the three-compartment chain model (Fig. 6). Fig. 12(d) was generated by varying the normalized leakage conductance γ_S. In Fig. 12(e), we vary the spike duration. As in the earlier experiments where spike duration was varied, we observe that bistability only occurs within a particular range of spike durations, and there is a unique value for which bistability is maximal. Finally, we see in Fig. 12(f) when varying the spike shape parameter p, that it is also more difficult to observe bistability for small values of p, and that a wider spike shape promotes bistability.

4. Discussion

In this work, we have presented a framework to study how complex dendritic tree structures can affect the firing dynamics of an LIF neuron that explicitly includes spike effects. The dendritic tree is modeled as a system of coupled passive compartments, i.e., a multicompartment model, which allows for flexibility in exploring complex branching topologies. We obtain the analytical solution and use it to derive a lower dimensional return map which completely characterizes the firing dynamics of the full system. As the return map is in the form of a matrix update equation, it provides a computationally efficient way to explore the effects of dendritic tree topology on firing dynamics when compared to simulations of the full system of coupled differential equations. Using the map, we explore how biophysical properties and dendritic tree architecture affect firing dynamics.
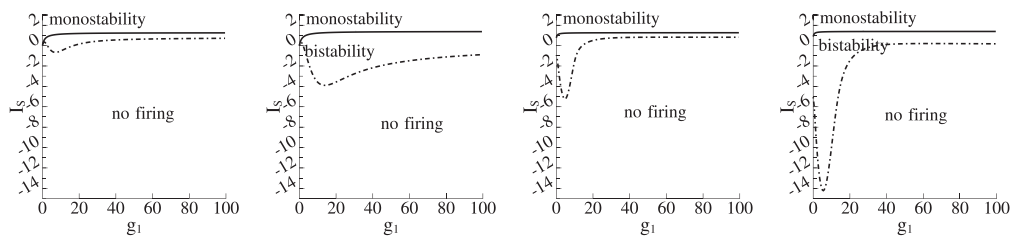

Fig. 11. Effect of g_1 in four compartments. Two-parameter bifurcation diagrams showing differences in stability with varying g_1, the normalized conductance parameter of the first connection, between different dendritic topologies of the four-compartment model (from left to right as in Fig. 10). The dashed-dotted line denotes the minimum injected somatic current needed to sustain oscillations, and any smaller value will result in the neuron becoming quiescent. The parameters used to produce these figures are $\alpha_i = 2$, $g_i = 4$, $I_i = 0$ for all i; $\beta_i = 0$, $\gamma_i = 1$ for all dendrites i and $\beta_S = 1$, $\gamma_S = 12$; $V_R = -2$, spike shape parameter $p = 0.05$, spike duration $T_a = 0.1$, with maximal spike potential $H = 80$.
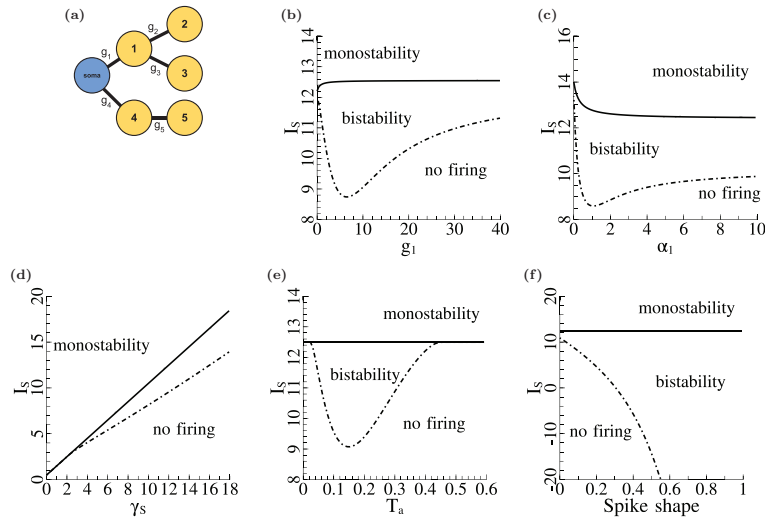
Fig. 12. Bifurcation analysis of a six-compartment neuron. Two-parameter bifurcation diagrams generated for a more complex dendritic topology, as shown in (a). In (b), the bifurcation diagram of injected somatic current I_S versus normalized conductance between the soma and first dendrite g_1 is shown, the ratio of the somatic area to that of the first dendrite α_1 is shown in (c), the normalized leakage conductance γ_S is shown in (d), the spike duration T_a is shown in (e), and the spike shape parameter p is shown in (f). Notice the similarities between these figures and the earlier figures. The parameters used to produce these diagrams are $\alpha_i = 5$, $g_i = 3$, $\gamma_i = 1$, $\gamma_S = 12$, $\beta_i = 0$, $\beta_S = 0$, $I_i = 0.4$, $V_R = -2$, $T_a = 0.1$, and a spike shape with maximal potential $H = 80$ and shape parameter $p = 0.05$.

As was first reported in [6], we also find that the addition of the dendritic tree can change the LIF model from Type 1 excitability to Type 2 excitability and induce bistability between periodic firing and the quiescent state. The mechanism responsible for the periodic behavior in the bistable regime is somatodendritic ping-pong. However, we go beyond the results of [6] by systematically examining how dendritic tree topology affects the appearance of this bistable behavior. We find that the structure of the dendritic tree can have significant quantitative effects on the bifurcation structure of the system, with branchier topologies tending to promote bistable behavior over unbranched chain topologies. We also show that this effect occurs even when the input conductance at the soma is held fixed, indicating that it is the dendritic tree topology that is mainly responsible for this quantitative change in the bifurcation structure. Lastly, we demonstrate how our framework can be used to explore how biophysical properties affect the firing dynamics of a neuron with a more complex dendritic tree topology.

Previous studies of multi-compartment LIF neurons have found that the addition of the passive dendrite can have interesting effects on firing dynamics [4,16,20]. In particular, these studies found that the addition of the dendrite can both delay the onset of oscillations as the input level is increased and also decrease the firing frequency at a given input level. However, as both of these studies did not include the effect of the somatic spike on the dendritic compartment, the bistable dynamics that we observe here (and also in [6]) were not observed.

The mechanism for periodic firing in the bistable regime results from a ping-pong action between the somatic and proximal dendritic potentials. This somatodendritic ping-pong has been observed in multi-compartment neuron models endowed with nonlinear ionic currents [21–25]. In this case, it was shown that somatodendritic ping-pong is responsible for the burst of action potentials observed during bursting activity [21]. Although we have not observed any bursting-like activity in our model, it would be interesting to explore whether the inclusion of a slow outward current in a proximal dendritic compartment might allow the model to exhibit bursting. However, this would rely mainly on simulations as the inclusion of any nonlinear currents would preclude an analytical solution. Indeed, in a large computational study, van Ooyen et al. [3] showed that when nonlinear ionic currents are included, dendritic topology can change

the type of firing from regular to bursting. Nonetheless, the simplicity of our current framework allows us to go beyond [21] to explore how structural and biophysical features of the dendritic tree interact with aspects of the somatic spike to either promote or inhibit somatodendritic ping-pong.

Similar to [6], we find that the main requirement for the appearance of somato-dendritic ping-pong is that the proximal dendritic compartment is sufficiently depolarized after a somatic spike so as to bring the somatic potential back above threshold. As such, it seems reasonable to expect that similar behavior can occur in a system where the soma is endowed with nonlinear Hodgkin–Huxley (HH) type ionic currents. However, our findings suggest that both the size (amplitude and duration) of the somatic spike as well as the rate of repolarization of the soma must be sufficiently large in order for ping-ponging to occur in a system with a passive dendritic tree. For standard HH-type ionic currents, it can be difficult to discern which combinations of parameters need to be altered in order to change specific features of the spike. The inclusion of active currents, such as a persistent sodium current, in the dendritic compartments (or even the inclusion of dendritic spines which may contain high densities of sodium channels [26]) can possibly alleviate the need to tweak the somatic spike properties and allow for a greater depolarization of the dendrite after a somatic spike, thus making it easier for the ping-pong effect to occur. Future work will be to explore how the type of somatic model one chooses changes the dendritic properties necessary for the ping-pong effect to occur. However, this would again rely primarily on the use numerical simulations.

Previous analytical approaches to exploring how dendritic topology affects the function of passive dendrites have relied on a Green's (or linear response) function approach [11–13,16,27]. These approaches provide a computationally efficient way to determine how the membrane potential of dendritic trees responds to time-varying inputs. Furthermore, the Green's function approach can be extended to dendritic trees with weakly nonlinear (or resonant) membrane dynamics [13] and also pairs of dendritic trees coupled via gap junctions [27]. Our current framework nicely complements these approaches as the linearity assumption of the Green's function approach prohibits the inclusion of any nonlinear spike-generating mechanism. Thus, future work will be to incorporate time-varying inputs into our approach as well as explore the effects of weakly nonlinear dendrites.

Although much recent research has focused on the role of nonlinear ionic currents in dendrites [28,29], it is important to note that in some neurons such as cerebellar stellate cells and hippocampal fast-spiking basket cells, dendrites express sodium channels at low density, if at all [30,31]. Thus, the dendrites of these cells will be well-modeled by passive dynamics. Furthermore, exploring passive properties of dendritic trees is important as they provide the fundamental substrate for dendritic dynamics [32]. Indeed, as we have shown here, even in neurons endowed with only passive dendritic trees, the interaction of passive dendritic tree properties and somatic spiking dynamics can significantly alter the firing dynamics of the system, leading to bistability between periodic firing and quiescence. As this type of behavior has been observed in parts of the central nervous system ranging from the spinal cord [33] to the neocortex [34] and is hypothesized to be closely related to short-term memory [35], understanding the various neuronal properties that lead to this behavior is of vital importance.

Acknowledgments

Appendix A

A.1. Generalization to arbitrary dendritic topologies

Extending our chain and branch models, we can represent any multi-compartment neuron with multiple passive connections using our matrix formulation. This generalization will show that our analysis of the general matrix form of our model is extendable to arbitrary dendritic topologies. The coefficient matrix A^{NS} can be decomposed into a sum of matrices:

$$A^{NS} = L + \sum_{i \neq j} \mathbb{1}\{i \text{ is connected to } j\} \cdot C_{i,j}. \tag{38}$$

The first matrix L is a diagonal matrix representing the intrinsic leak current for each compartment where the mth diagonal element is $-\gamma_m$ for all m and the matrix is zero everywhere else.

$$L = \begin{bmatrix} -1 & 0 & 0 & \cdots & 0 \\ 0 & -\gamma_2 & 0 & \cdots & 0 \\ 0 & 0 & -\gamma_3 & \cdots & 0 \\ \vdots & \vdots & \vdots & \ddots & \cdots \\ 0 & 0 & 0 & \cdots & -\gamma_S \end{bmatrix}. \tag{39}$$

The term $\mathbb{1}\{i \text{ is connected to } j\}$ indicates whether a connection exists between compartment i and compartment j. If such a connection exists, then $\mathbb{1}\{i \text{ is connected to } j\} = 1$, otherwise it is zero. The term $C_{i,j}$ is a matrix that provides additional terms which characterize the transfer of charge across the connection between compartments i and j.

$$C_{i,j} = \begin{bmatrix} \ddots & & & & \\ & -\alpha_i g_k & \cdots & \alpha_i g_k & \\ & \vdots & \ddots & \vdots & \\ & \alpha_j g_k & \cdots & -\alpha_j g_k & \\ & & & & \ddots \end{bmatrix}. \tag{40}$$

The element at position (i, i) is $-\alpha_i g_k$, the element at position (j, j) is $-\alpha_j g_k$, the element at position (i, j) is $\alpha_i g_k$, the element at position (j, i) is $\alpha_j g_k$, and the matrix is zero everywhere else, where k represents the unique index of the connection. As a concrete example to better illustrate this decomposition, we show how A^{NS}_{branch} can be decomposed into L and $C_{i,j}$ where the number of dendrites is 2:

$$A^{NS}_{branch} = \begin{bmatrix} -1 - \alpha_1 g_1 & 0 & \alpha_1 g_1 \\ 0 & -\gamma_2 - \alpha_2 g_2 & \alpha_2 g_2 \\ g_1 & g_2 & -\gamma_S - g_1 - g_2 \end{bmatrix}$$
$$= L + C_{S,1} + C_{S,2}, \quad \text{where:}$$
$$L = \begin{bmatrix} -1 & 0 & 0 \\ 0 & -\gamma_2 & 0 \\ 0 & 0 & -\gamma_S \end{bmatrix}, \quad C_{S,1} = \begin{bmatrix} -\alpha_1 g_1 & 0 & \alpha_1 g_1 \\ 0 & 0 & 0 \\ 1 \cdot g_1 & 0 & -1 \cdot g_1 \end{bmatrix},$$
$$C_{S,2} = \begin{bmatrix} 0 & 0 & 0 \\ 0 & -\alpha_2 g_2 & \alpha_2 g_2 \\ 0 & 1 \cdot g_2 & -1 \cdot g_2 \end{bmatrix}. \tag{41}$$

Notice that for biophysically-plausible values for the parameters, the absolute value of the diagonal element in each row of $C_{i,j}$ is equal to the absolute value of the non-diagonal elements. Additionally, since L_{NS} has no zero elements in the diagonal, then A^{NS} must be strictly diagonally dominant. Therefore, A^{NS} is nonsingular, diagonalizable, and Hurwitz stable (i.e. the real parts of the eigenvalues are strictly negative) [36]. The argument can also be extended to the spiking system, as A^S is also strictly diagonally-dominant.

Also note that for biophysically-plausible parameter values, the corresponding digraph of the matrix A^{NS} is strongly connected if and only if the compartments of the neuron are connected (the topology of the digraph is identical to that of the compartments in the neuron). Therefore, the matrix A^{NS} is irreducible [37]. Although the model can be extended to include cycles in the dendritic structure, we restrict our analysis to tree-like dendritic topologies. Thus, due to the construction of the $C_{i,j}$ matrices, both A^{NS} and A^S are sign-symmetric, and are similar to real symmetric matrices [38]. So if there are no cycles among the compartments, then all of the eigenvalues of A^{NS} and A^S are real. Note that even with a single cycle among the compartments, it is possible to obtain complex eigenvalues with biophysically-plausible parameters.

A.2. Input conductance properties in our model

Note that even when comparing neurons of different topologies, the threshold somatic current for monostability is the same across all topologies when b_i and $\gamma_S \beta_S$ do not change. Thus, if all dendritic injected currents I_i and all β_i (including β_S) are zero, then the threshold somatic current that determines whether the neuron is monostable is the same, regardless of the dendritic topology.

$$I_{S,th} = \frac{V_{th} + \sum_{i=1}^{n} [(A^{NS})^{-1}]_{\{n+1,i\}} b_i}{[A^{NS}]_{\{n+1,n+1\}}} - \gamma_S \beta_S. \tag{42}$$

We can express the input conductance recursively, as a function of the input conductance of subtrees. The input conductance of a tree can be defined as the input conductance of the multi-compartment LIF neuron whose soma is the root compartment of the tree. We first consider a neuron whose soma is connected to k dendritic trees, each of arbitrary topology, which we label T^i with root compartment a_i, see Fig. 13. Let A^{NS}_i be the A^{NS} matrix for T^i. Let b be the somatic
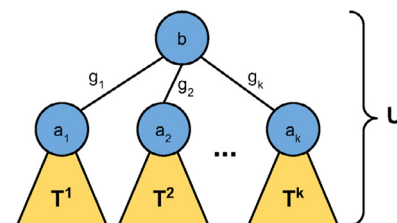

Fig. 13. Subtrees in the dendritic tree. The input conductance of the neuron U can be expressed as a function of the input conductance of each subtree $T^1,...,T^k$.

compartment which we connect to all a_i, and is the soma of the new tree U. So α_i and α_b are the normalized size parameters of a_i and b, respectively, and g_i is the normalized conductance of the connection between a_i and b in U.

$$
A_U^{NS} =
\begin{bmatrix}
A_{1*}^{NS} & \mathbf{0} & \mathbf{0} & \begin{matrix} 0 \\ \vdots \\ 0 \\ \alpha_1 g_1 \end{matrix} \\
\mathbf{0} & \ddots & \mathbf{0} & \begin{matrix} \vdots \\ 0 \end{matrix} \\
\mathbf{0} & \mathbf{0} & A_{k*}^{NS} & \begin{matrix} \vdots \\ 0 \\ \alpha_k g_k \end{matrix} \\
\begin{matrix} 0 & \dots & 0 & \alpha_b g_1 \end{matrix} & \dots & \begin{matrix} 0 & \dots & 0 & \alpha_b g_k \end{matrix} & -\gamma_b - \alpha_b \sum_{i=1}^{k} g_i
\end{bmatrix},
\tag{43}
$$

where A_{i*}^{NS} is the portion of the A_U^{NS} matrix that corresponds to the subtree T^i. Thus, A_{i*}^{NS} is identical to A_i^{NS} but with an additional $-\alpha_i g_i$ term in the diagonal element corresponding to the connection between compartments b and a_i (which we assume is the last diagonal element in A_i^{NS}). Let G_i be the input conductance of T^i, and so $G_{i*} = G_i + \alpha_i g_i$. Let $n+1$ be the total number of compartments of the tree U. We use blockwise matrix inversion, dividing A_U^{NS} into four submatrices: the top-left $n \times n$ block-diagonal matrix where each block is A_{i*}^{NS}, the top-right $n \times 1$ matrix, the bottom-left $1 \times n$ matrix, and the 1×1 element containing the term $-\gamma_b - \alpha_b \sum_{i=1}^{k} g_i$. We obtain an expression for the input conductance of the new tree U:

$$
G = \gamma_b + \alpha_b \sum_{i=1}^{k} g_i + \sum_{i=1}^{k} [0 \ \dots \ 0 \ \alpha_b g_i](A_{i*}^{NS})^{-1}
\begin{bmatrix} 0 \\ \vdots \\ 0 \\ \alpha_i g_i \end{bmatrix},
\tag{44}
$$

$$
= \gamma_b + \alpha_b \sum_{i=1}^{k} g_i - \alpha_b \sum_{i=1}^{k} \alpha_i g_i^2 G_{i*}^{-1},
\tag{45}
$$

$$
= \gamma_b + \alpha_b \sum_{i=1}^{k} \frac{g_i G_i}{G_i + \alpha_i g_i}.
\tag{46}
$$

Note that this expression is also valid for $k = 0$, in which case the input conductance of a single compartment is γ_b.

A.3. Effect of biophysical parameters on input conductance

We observe via the derivative of the expression in Eq. (46) that the input conductance is monotonically increasing with respect to the input conductances of the subtrees (this argument can be extended inductively to the input conductance of any subtree in the topology):

$$
\frac{\partial G}{\partial G_i} = \frac{\alpha_b \alpha_i g_i^2}{(G_i + \alpha_i g_i)^2},
\tag{47}
$$

is strictly positive given biophysically-plausible parameter values. Also note that the input conductance is monotonically increasing with respect to α_b, g_i, and γ_b: $\frac{\partial G}{\partial \alpha_b} = \sum_{i=1}^{k} \frac{g_i G_i}{G_i + \alpha_i g_i}$, $\frac{\partial G}{\partial \gamma_b} = 1$, and $\frac{\partial G}{\partial g_i} = \frac{\alpha_b G_i^2}{(G_i + \alpha_i g_i)^2} > 0$. This argument can be extended inductively to all biophysical parameters using the chain rule $\frac{\partial G}{\partial x} = \frac{\partial G}{\partial G_i} \frac{\partial G_i}{\partial x}$. Additionally, for a given set of fixed biophysical parameters, the input conductance increases monotonically with the number of dendrites.
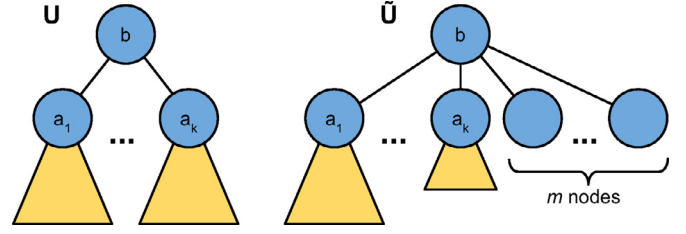

Fig. 14. Depiction of a neuron and a "flattened" neuron. Two LIF neurons are depicted. The neuron labeled U is identical to $\tilde{U}$ except that m compartments are removed from the subtree attached to compartment a_k in U and re-attached directly to the soma in $\tilde{U}$.

A.4. Input conductance and dendritic topology

Consider a dendritic tree U where the soma is connected to k dendritic trees, each labeled T_i. Consider another tree $\tilde{U}$ with the same structure as U except the subtree T^k has m fewer compartments, which are moved and directly attached to the soma (see Fig. 14). We will show by induction that $\tilde{U}$ has a strictly greater input conductance than U. From this, it will follow that the input conductance is maximized in the branch model and minimized in the chain model.

We compute the input conductance of the first tree U:

$$
G = \gamma_b + \alpha_b \sum_{i=1}^{k-1} \frac{g_i G_i}{G_i + \alpha_i g_i} + \alpha_b \frac{g_k G_k}{G_k + \alpha_k g_k},
\tag{48}
$$

$$
\leq \gamma_b + \alpha_b \sum_{i=1}^{k-1} \frac{g_i G_i}{G_i + \alpha_i g_i} + \alpha_b \frac{g_k(\gamma_k + \alpha_k S)}{\gamma_k + \alpha_k S + \alpha_k g_k},
\tag{49}
$$

where $S = \sum_{i=1}^{|T^k|} \frac{g_i^{(k)} \gamma_i^{(k)}}{\gamma_i^{(k)} + \alpha_i^{(k)} g_i^{(k)}}$ is the contribution to the input conductance of T^k from its dendritic compartments, assuming T^k has a branch-model architecture. Similarly, the input conductance of the second tree U_2 is:

$$
\tilde{G} = \gamma_b + \alpha_b \sum_{i=1}^{k-1} \frac{g_i G_i}{G_i + \alpha_i g_i} + \alpha_b \frac{g_k \tilde{G}_k}{\tilde{G}_k + \alpha_k g_k} + \alpha_b S_m,
\tag{50}
$$

where $S_m = \sum_{i=1}^{m} \frac{g_i^{(k)} \gamma_i^{(k)}}{\gamma_i^{(k)} + \alpha_i^{(k)} g_i^{(k)}}$ and $\tilde{G}_k$ is the input conductance of the tree T^k after the removal of m compartments. Note that $G_k = \gamma_k + \alpha_k S \leq \tilde{G}_k + \alpha_k S_m$ since G_k is maximal when T^k has a branch-model architecture. We now compute an upper bound on the difference between the input conductances:

$$
G - \tilde{G} \leq \alpha_b \frac{g_k(\gamma_k + \alpha_k S)}{\gamma_k + \alpha_k S + \alpha_k g_k} - \alpha_b \frac{g_k \tilde{G}_k}{\tilde{G}_k + \alpha_k g_k} - \alpha_b S_m,
\tag{51}
$$

$$
= \alpha_b \frac{\alpha_k g_k^2(\gamma_k + \alpha_k S) - \alpha_k g_k^2 \tilde{G}_k - S_m(\tilde{G}_k + \alpha_k g_k)(\gamma_k + \alpha_k S + \alpha_k g_k)}{(\tilde{G}_k + \alpha_k g_k)(\gamma_k + \alpha_k S + \alpha_k g_k)},
\tag{52}
$$

$$
\leq \alpha_b \frac{\alpha_k^2 g_k^2 S_m - S_m(\tilde{G}_k + \alpha_k g_k)(\gamma_k + \alpha_k S + \alpha_k g_k)}{(\tilde{G}_k + \alpha_k g_k)(\gamma_k + \alpha_k S + \alpha_k g_k)},
\tag{53}
$$

$$
\leq -\alpha_b \frac{\gamma_k \tilde{G}_k + \alpha_k g_k \gamma_k + \alpha_k \tilde{G}_k S + \alpha_k^2 g_k S + \alpha_k g_k \tilde{G}_k}{S_m(\tilde{G}_k + \alpha_k g_k)(\gamma_k + \alpha_k S + \alpha_k g_k)},
\tag{54}
$$

$$
< 0.
\tag{55}
$$

We have shown that if $m > 0$ compartments are moved from any subtree and connected to the soma, the resulting neuron will have a strictly greater input conductance. Therefore, flatter and more highly
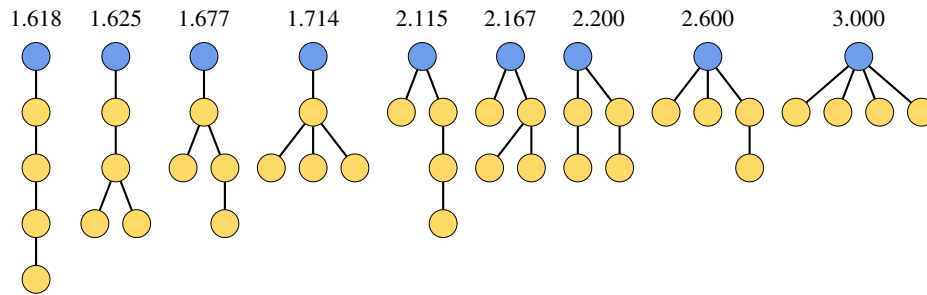
Fig. 15. Topologies of the five-compartment model. The topologies are sorted by their input conductance.

branched dendritic architectures will have larger input conductances, as is visible in Fig. 15.

References

[1] C. Koch, I. Segev, The role of single neurons in information processing, Nature 3 (2000) 1171–1177.
[2] Z.F. Mainen, T.J. Sejnowski, Influence of dendritic structure on firing pattern in model neocortical neurons, Nature 382 (1996) 363–366.
[3] J. van Ooyen, A. Duijnhouwer, M.W.H. Remme, J. van Pelt, The effect of dendritic topology on firing patterns in model neurons, Network: Comput. Neural Syst. 13 (2002) 311–325.
[4] P. Lánský, R. Rodriguez, The spatial properties of a model neuron increases its coding range, Biol. Cybern. 81 (1999) 161–167.
[5] M.A. Schwemmer, T.J. Lewis, Effects of dendritic load on the firing frequency of oscillating neurons., Phys. Rev. E 83 (2011) 031906.
[6] M.A. Schwemmer, T.J. Lewis, Bistability in a leaky integrate-and-fire neuron with a passive dendrite., SIAM J. Appl. Dyn. Syst. 11 (1) (2012) 507–539.
[7] W. Rall, Membrane time constants of motoneurons, Science 126 (1957) 454.
[8] W. Rall, Branching dendritic trees and motoneuron membrane resistivity, Exp. Neurol. 2 (1959) 491–527.
[9] W. Rall, Membrane potential transients and membrane time constant of motoneurons, Exp. Neurol. 2 (1960) 503–532.
[10] J. Duijnhouwer, M.W.H. Remme, A. van Ooyen, J. van Pelt, Influence of dendritic topology on firing patterns in model neurons, Neurocomputing 38–40 (2001) 183–189.
[11] L.F. Abbott, E. Farhi, S. Gutmann, The path integral for dendritic trees., Biol. Cybern. 66 (1) (1991) 49–60.
[12] L.F. Abbott, Simple diagrammatic rules for solving dendritic cable problems, Physica A 185 (1) (1992) 343–356.
[13] S. Coombes, Y. Timofeeva, C.-M. Svensson, G.J. Lord, K. Josić, S.J. Cox, C.M. Colbert, Branching dendrites with resonant membrane: a "sum-over-trips" approach, Biol. Cybern. 97 (2) (2007) 137–149.
[14] L.F. Abbott, Lapicque's introduction of the integrate-and-fire model neuron (1907), Brain Res. Bull. 50 (5–6) (1999) 303–304.
[15] A.L. Hodgkin, The local electric changes associated with repetitive action in a non-medullated axon, J. Physiol. 107 (1948) 165–181.
[16] P.C. Bressloff, J.G. Taylor, Dynamics of compartmental model neurons, Neural Networks 7 (6) (1994) 1153–1165.
[17] P.C. Bressloff, S. Coombes, Physics of the extended neuron, J. Mod. Phys. B 11 (1997) 2343–2392.
[18] R. Traub, R. Wong, R. Miles, H. Michelson, A model of a ca3 hippocampal pyramidal neuron incorporating voltage-clamp data on intrinsic conductances, J. Neurophysiol. 66 (1991) 635–649.
[19] T.J. Dekker, Finding a zero by means of successive linear interpolation, in: B. Dejon, P. Henrici (Eds.), Constructive Aspects of the Fundamental Theorem of Algebra, Wiley Interscience, London, 1969.
[20] P. Bressloff, Dynamics of a compartmental model integrate-and-fire neuron with somatic potential reset, Physica D 80 (1995) 399–412.
[21] A. Bose, V. Booth, Bursting in 2-compartment neurons: a case study of the Pinsky-Rinzel model, in: S. Coombes, P. Bressloff (Eds.), Bursting: The Genesis of Rhythm in the Nervous System, World Scientific, 2005, pp. 123–144.
[22] B. Doiron, C. Laing, A. Longtin, Ghostbursting: a novel neuronal burst mechanism, J. Comput. Neurosci. 12 (2002) 5–25.
[23] C. Laing, A. Longtin, A two-variable model of somatic-dendritic interactions in a bursting neuron, Bull. Math. Biol. 64 (5) (2002) 829–860.
[24] P.F. Pinsky, J. Rinzel, Intrinsic and network rhythmogenesis in a reduced Traub model for CA3 neurons, J. Comput. Neurosci. 1 (1994) 39–60.
[25] X.J. Wang, Fast firing and short-term synaptic plasticity: a model of neocortical chattering neurons, Neuroscience 89 (2) (1999) 347–362.
[26] D. Tsay, R. Yuste, Role of dendritic spines in action potential backpropagation: a numerical simulation study, J. Neurophysiol. 88 (5) (2002) 2834–2845.
[27] Y. Timofeeva, S. Coombes, D. Michieletto, Gap junctions, dendrites and resonances: a recipe for tuning network dynamics, J. Math. Neurosci. 3 (2013) 15.
[28] D. Johnston, R. Narayanan, Active dendrites: colorful wings of the mysterious butterflies, Trends Neurosci. 31 (6) (2008) 309–316.
[29] I. Segev, M. London, Untangling dendrites with quantitative models, Science 290 (5492) (2000) 744–750.
[30] H. Hu, M. Martina, P. Jonas, Dendritic mechanisms underlying rapid synaptic activation of fast-spiking hippocampal interneurons, Science 327 (2010) 52–58.
[31] M.H. Myoga, M. Beierlein, W. Regehr, Somatic spikes regulate dendritic signaling in small neurons in the absence of backpropagating action potentials, J. Neurosci. 29(24) (2009) 7803–7814.
[32] M. London, M. Häusser, Dendritic computation, Annu. Rev. Neurosci. 28 (2005) 503–532.
[33] Y. Prut, E.E. Fetz, Primate spinal interneurons show pre-movement instructed delay activity, Nature 401 (6753) (1999) 590–594.
[34] J.M. Fuster, Memory in the Cerebral Cortex, MIT Press, Cambridge, MA, 1996.
[35] R. Cossart, D. Aronov, R. Yuste, Attractor dynamics of network up states in the neocortex, Nature 423 (6937) (2003) 283–288.
[36] F.N. Dafchahi, Computing of signs of eigenvalues for diagonally dominant matrix for inertia problem., Appl. Math. Sci., Ruse 2 (29-32) (2008) 1487–1491.
[37] A. Berman, R.J. Plemmons, Nonnegative Matrices in the Mathematical Sciences (Classics in Applied Mathematics), Society for Industrial Mathematics, 1987.
[38] S. Parter, On the eigenvalues and eigenvectors of a class of matrices, J. Soc. Ind. Appl. Math. 8 (2) (1960) 376–388.